



# Momentum-space-resolved measurements using oblique electron cyclotron emission for the validation of the quasi-linear theory of electron cyclotron current drive

S S Denk<sup>1,2</sup> , R Fischer<sup>1</sup>, E Westerhof<sup>3</sup>, T Luda di Cortemiglia<sup>1,4</sup> , J Hobirk<sup>1</sup> , O Maj<sup>1</sup>, E Poli<sup>1</sup>, S K Nielsen<sup>5</sup> , J Rasmussen<sup>5</sup> , M Stejner<sup>5</sup>, J Stober<sup>1</sup> , U Stroth<sup>1,6</sup>, W Suttrop<sup>1</sup>, M Willensdorfer<sup>1</sup>  and the ASDEX Upgrade Team<sup>7</sup>

<sup>1</sup> Max-Planck-Institut für Plasmaphysik, D-85748 Garching, Germany

<sup>2</sup> Present address: Plasma Science and Fusion Center, Massachusetts Institute of Technology, Cambridge, MA 02139, United States of America

<sup>3</sup> DIFFER—Dutch Institute for Fundamental Energy Research, De Zaale 20, Eindhoven, AJ 5612, The Netherlands

<sup>4</sup> Aix-Marseille Université, CNRS, PIIM UMR 7345, 13397 Marseille, France

<sup>5</sup> Technical University of Denmark, Department of Physics, Kgs. Lyngby, Denmark

<sup>6</sup> Physik-Department E28, Technische Universität München, 85748 Garching, Germany

E-mail: [denk@mit.edu](mailto:denk@mit.edu)

Received 22 July 2020, revised 29 September 2020

Accepted for publication 15 October 2020

Published 10 November 2020



CrossMark

## Abstract

Electron cyclotron resonance heating (ECRH) can drive large current densities through electron cyclotron current drive (ECCD). ECCD is expected to be crucial for high-performance plasmas in future fusion reactors like ITER and DEMO, making the current drive efficiency of ECCD a critical design parameter for future reactors. In present-day devices, good agreement between measured and predicted current drive efficiency has been found. However, to ensure the reliability in future machines, a direct validation of the electron momentum distribution function is needed.

As a first step towards this goal, we present in this paper oblique electron cyclotron emission (ECE) measurements of a low-density plasma in the ASDEX Upgrade tokamak. Two oblique ECE diagnostics are used to allow the simultaneous measurements of electrons streaming co- and counter-directionally with the plasma current. Predictions for the distribution function are

<sup>7</sup> ASDEX Upgrade team: See author list of H Meyer *et al* 2019 Nucl. Fusion **59** 112014.

<sup>8</sup> See <http://www.euro-fusionscipub.org/eu-im>.



Original Content from this work may be used under the terms of the [Creative Commons Attribution 4.0 licence](https://creativecommons.org/licenses/by/4.0/). Any further distribution of this work must maintain attribution to the author(s) and the title of the work, journal citation and DOI.

computed with the bounce-averaged Fokker-Planck code RELAX.<sup>9</sup> To allow direct comparison with the measurements, synthetic radiation temperatures are computed with the code ECRad.<sup>10</sup> Good agreement is found if radial transport occurring predominantly at low electron energies is included.

We demonstrate that oblique ECE diagnostics measure the electron distribution function directly at the ECRH deposition site in phase space. Furthermore, they are sensitive to the abundance of pitch-angle scattered electrons that reduce the ECCD efficiency. Limitations and uncertainties of the measurements and the modeling are discussed.

Keywords: electron cyclotron current drive, electron cyclotron emission, non-thermal electron velocity distribution

(Some figures may appear in colour only in the online journal)

## 1. Introduction

Electron cyclotron resonance heating (ECRH) is a technique that utilizes focused, MW-strong microwave beams to heat a magnetized plasma. If the power is injected obliquely to the magnetic field, the microwave power is deposited onto electrons streaming in a particular direction. This technique is called electron cyclotron current drive (ECCD) [1], as it can drive significant and localized currents inside the plasma. Both qualities are highly desirable for a fusion power plant, and most current and planned fusion reactors have an ECRH system [2–10].

A critical quantifier for the design of ECRH systems is the current drive efficiency, i.e. how much current can be driven per unit of absorbed power. In most present and planned fusion reactors based on the magnetic confinement concept, the deposited amount of power density is small enough such that the magnitude of the driven current scales linearly with respect to the injected power [11, 12]. This implies that the changes in the electron distribution function caused by ECRH are minimal. If, however, the energy flux from the beam to the plasma is sufficiently large, or electron density ( $n_e$ ) is sufficiently low [11], the perturbation of the distribution function becomes large enough to affect the absorption of electron cyclotron waves by the plasma, rendering the current drive efficiency non-linear with respect to the input power.

Regardless of whether the ECCD response is linear or not, the driven current is given by the steady-state electron distribution function subject to collisions and electron cyclotron diffusion due to the ECRH absorption [13]. In addition to this, radial transport can play a significant role [11, 14] and, in tokamaks, so can the parallel electric field [15]. Several studies have confirmed the overall accuracy of the theoretical model for ECCD [16–21]. However, none of the measurement techniques employed in these studies are able to resolve the electron distribution function in momentum space directly at the site of microwave absorption. To ensure the reliability of

the theoretical model for ECCD, it is desirable to verify the predicted electron momentum distribution function directly, instead of only the current profile derived from it.

This paper presents a first step to confirm the quasi-linear theory for ECCD using oblique electron cyclotron emission (ECE) measurements capable of resolving the electron distribution function at the ECRH deposition site in the phase space spanned by a radial coordinate and cylindrical momentum space. Oblique ECE diagnostics have already proven to be a useful tool for the assessment of the current drive efficiency of lower hybrid current drive [22], which is another wave-based scheme for electron heating. Furthermore, qualitative studies of non-thermal electron distributions have been made with oblique ECE [23–26], and an oblique ECE system is planned for ITER [27].

In this paper, the measurements of ASDEX Upgrade (ASDEX Upgrade) discharge #35 662 taken by two oblique ECE diagnostics are compared to synthetic ECE spectra computed with the electron cyclotron radiation transport model for advanced data analysis (*ECRad*) [28]. For the computation of the electron distribution functions, the quasi-linear Fokker-Planck code RELAX [29] is used. The current drive and power deposition profiles obtained with RELAX are compared against linear calculations with Gray [30] and TOR-BEAM [31, 32]. Since radial transport can be a significant factor for the current drive profile [11, 14, 20], three different models for the momentum dependence of the radial diffusion coefficient are investigated. Lastly, the phase-space sensitivity of radial and oblique ECE measurements is discussed.

The paper is structured into six sections. First, the oblique ECE system at ASDEX Upgrade and the design of discharge #35 662 are presented. Next, the data analysis yielding the plasma profiles and the equilibrium is briefly discussed, and the modeling of the electron distribution function and the synthetic ECE signals is presented. In section 4, the measurements of two oblique ECE systems and a radial ECE system are compared to the forward-modeled radiation temperatures ( $T_{\text{rad}}$ ) for four empirical models for the radial transport coefficient. Section 5 discusses the phase-space sensitivity of the radial ECE and the two oblique systems. Section 6 addresses the limitations of this study. The paper concludes with a summary in section 7.

<sup>9</sup>E Westerhof *et al*, Rijnhuizen report, 1992.

<sup>10</sup>S Denk *et al*, Computer Physics Communications, p. 107175, 2020.

## 2. Diagnostic system and discharge scenario

This section gives a short overview of the oblique ECE system at ASDEX Upgrade and describes ASDEX Upgrade discharge #35 662, which will be discussed in this paper.

### 2.1. Oblique ECE system

The oblique ECE measurements are performed with the radiometers used by the collective Thomson scattering (CTS) system [33, 34]. It uses ECRH wave guides and launchers for the transmission, which allows for a highly flexible viewing geometry. The CTS diagnostic consists of two independent radiometers, each connected to one of the ECRH beam lines. The radiometer ‘CTA’ features 50 irregularly spaced channels ranging from 4.4 GHz below to 4.5 GHz above 105 GHz, which is the frequency of the gyrotron used in the experiment. The second radiometer ‘CTC’ has 42 ECE channels that are spaced slightly more narrowly than the ‘CTA’ system. The lowest measured frequency is 3.0 GHz below the gyrotron frequency and the highest 3.0 GHz above it. CTS and conventional ECE diagnostics are multi-channel heterodyne radiometers. One important difference is that the signal strength of CTS is significantly lower than that of ECE, and so must be strongly amplified. To protect the electronics from correspondingly amplified non-CTS signals at the same frequencies, voltage-controlled variable attenuators are integrated into both receivers. They allow for adjustable attenuation in the range of 0 to  $-40$  dB. Both receivers are equipped with two rotatable wire grids allowing for precise mode filtering even at oblique observation angles. For the discussed experiments, X-mode polarization was selected.

The diagnostic was not individually calibrated for the experiment discussed in this paper. Since an absolute calibration of the diagnostic is necessary for the validation of ECCD-theory, the diagnostic is cross-calibrated against the electron temperature ( $T_e$ ) profiles obtained with a conventional ECE system, which in turn is calibrated against hot and cold black body radiators [35]. How the cross-calibration is performed is discussed in appendix A. The calibrated measurements of this diagnostic are averaged over 10 ms. The error bars shown in figures indicate one standard deviation of the statistical uncertainty plus one standard deviation of estimated systematic uncertainty derived from the cross calibration as discussed in reference [28].

### 2.2. Discharge scenario

This paper discusses the oblique ECE measurements of the ASDEX Upgrade discharge #35 662 with a toroidal magnetic field  $B_t = -1.8$  T and a plasma current of  $I_p = 460$  kA. A single gyrotron at 105 GHz, and a power of 490 kW is used. Due to the toroidal injection angle of  $-20^\circ$ , the gyrotron drives counter-ECCD (short ctr-ECCD).

The discharge can be structured into two sections: A phase without ECRH for the cross-calibration of the oblique ECE utilizing a neutral beam injection (NBI) power ramp

and a phase in which ECCD drives the electron momentum distribution non-thermal. Figure 1 shows a time trace of  $T_e$ ,  $n_e$ , and the ECRH and NBI heating power. The period over which the calibration is performed is shaded in cyan, and the time-point  $t = 3.84$  s discussed in this paper is marked with a vertical red line.

The toroidal angles of the oblique ECE arrays are  $+20^\circ$  for ‘CTA’ and  $-20^\circ$  for ‘CTC’. A top view of the beam paths is shown in figure 2(b). It is noteworthy that, even though ‘CTC’ is the array with the same toroidal angle as the ECRH, it is sensitive to co-streaming electrons. Since the wave vector of ECE is rotated by  $180^\circ$  with respect to the ECRH wave vector, the Doppler-shift also has an opposite sign. Accordingly, ‘CTA’ is the array directly sensitive to the counter-streaming electrons subject to ECCD. In the scope of this paper, the sensitivity to either co- and ctr-streaming electrons is the most important property of these two diagnostics. Therefore, they will be referred to as ctr-ECE (‘CTA’) and as co-ECE (‘CTC’) from here on out. The sensitivity of the two arrays is discussed in detail in section 5.

The magnetic equilibrium is shown in figure 2, which also indicates the volume of sight (VOS) of the radial ECE [36], the two oblique ECE receivers, and the ECRH beam. Figure 2(b) contains the corresponding top view. The ‘warm resonance positions’ [37] (not depicted), i.e. the maxima of the birthplace distributions [37, 38] of the two oblique ECE diagnostics lie close to the flux surfaces onto which the gyrotron deposits its power (see section 5).

## 3. Data analysis and modeling

A multitude of measurements and codes is needed in order to predict the synthetic ECE spectra during ECCD. The flow chart in figure 3 illustrates the data flow and the interdependencies between the different codes. This section guides the reader through this flowchart from the top to the bottom, The relevant sections are indicated on the flow chart.

### 3.1. Data analysis

Computing the electron momentum distribution functions requires kinetic profiles ( $T_e$  and  $n_e$ ), a magnetic equilibrium, and an estimate for the effective ion charge profile ( $Z_{\text{eff}}$ ). The kinetic profiles and the equilibrium are also needed for the calibration of the oblique ECE (see appendix A). All quantities are derived from the measurements by the means of Integrated Data Analysis (IDA) [39].

The following set of diagnostics is considered in IDA:

- » ECE [36] for  $T_e$ ;
- » Thomson scattering [40] for  $T_e$  and  $n_e$ ;
- » Plasma interferometry [41] for  $n_e$ ;
- » Lithium beam emission spectroscopy [42] for  $n_e$ .

The IDA analysis is performed twice, first with a magnetic equilibrium provided by the CLISTE code [43], and then with the magnetic equilibrium reconstructed by the integrated data

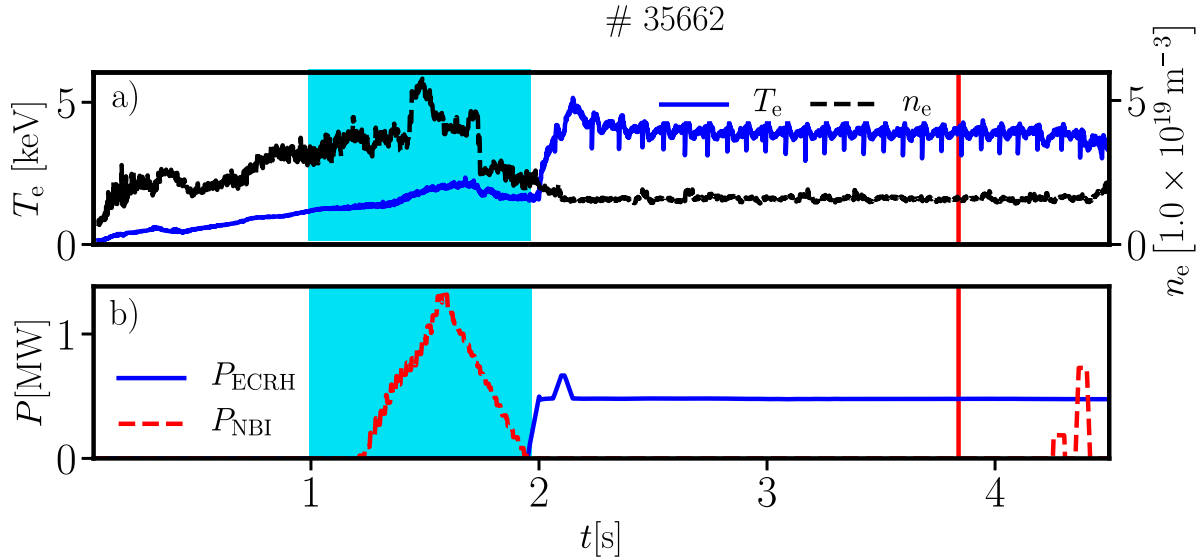


**Figure 1.** (a) Time evolution of  $T_e$  and  $n_e$  at the magnetic axis. (b) NBI and ECRH power for discharge #35 662. The phase designated for the cross-calibration of the oblique ECE is shaded cyan. The point discussed in this paper is marked by the red vertical line.

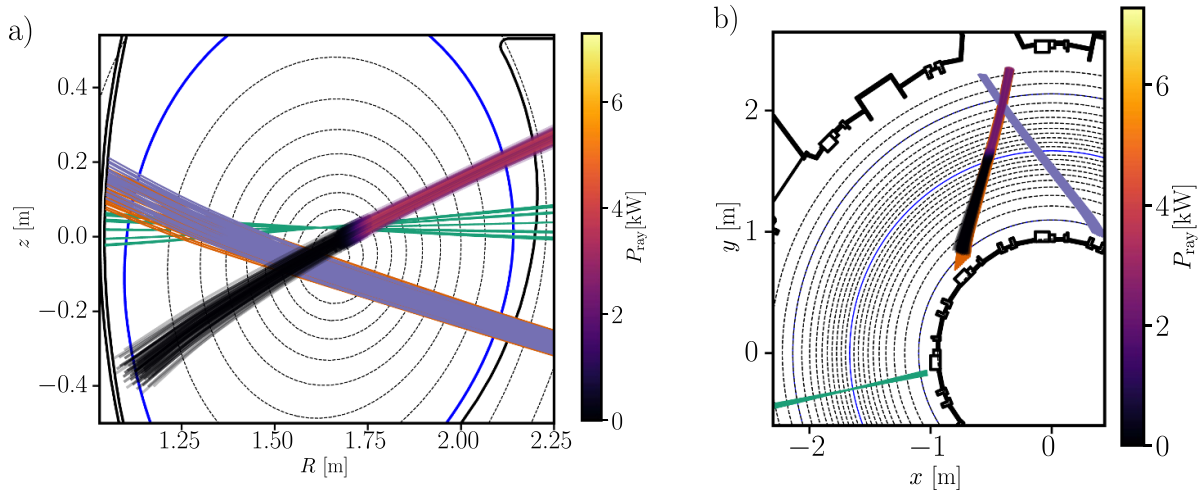


**Figure 2.** Plasma shape and VOS of the ECE diagnostics and trajectory of the ECRH beam for discharge #35 662. The VOS of the radial ECE is shown in turquoise, and the VOS of the oblique ECE are blue (ctr-ECE or ‘CTA’) and orange (co-ECE or ‘CTC’). Please note that they overlap in (a) and that the VOS of the co-ECE overlaps with the ECRH beam in (b). The beam trajectory of the ECRH is color-coded to indicate the intensity of the individual rays. The separatrix and the magnetic axis are marked in dark blue. Figure (a) shows a poloidal cross section and figure (b) the corresponding top view.

analysis equilibrium (IDE) code [44]. This two-step process is necessary because the IDE code requires the kinetic profiles as an input. It also needs the ion pressure profile, which is obtained from charge exchange recombination measurements [45]. This diagnostic directly delivers the ion temperature ( $T_i$ ) profile during NBI power injection. Additionally, it enables Bremsstrahlung measurements from which the  $Z_{\text{eff}}$  profile can be estimated [46]. From the  $Z_{\text{eff}}$  and the  $n_e$  profiles, the ion density profile is derived. Lastly, IDE also needs the fast ion pressure, which is derived with the RABBIT code [47], and the ECCD profile, which is computed with TORBEAM [31, 32].

To achieve a reasonable match between measurements and theoretical predictions, the equilibrium obtained with IDE is empirically shifted downwards by a cm. This downward shift

agrees with the uncertainties of the equilibrium position and the uncertainties of the ECRH deposition location. This is clarified in section 6.

### 3.2. Electron cyclotron current drive

The electron momentum distribution functions are computed with the RELAX code [29]. It is a bounce-averaged Fokker-Planck code that takes into account:

- Quasi-linear electron cyclotron damping;
- Weakly relativistic, momentum-conserving collisions via a truncated collision operator;
- The parallel electric field;
- Radial diffusion [14];

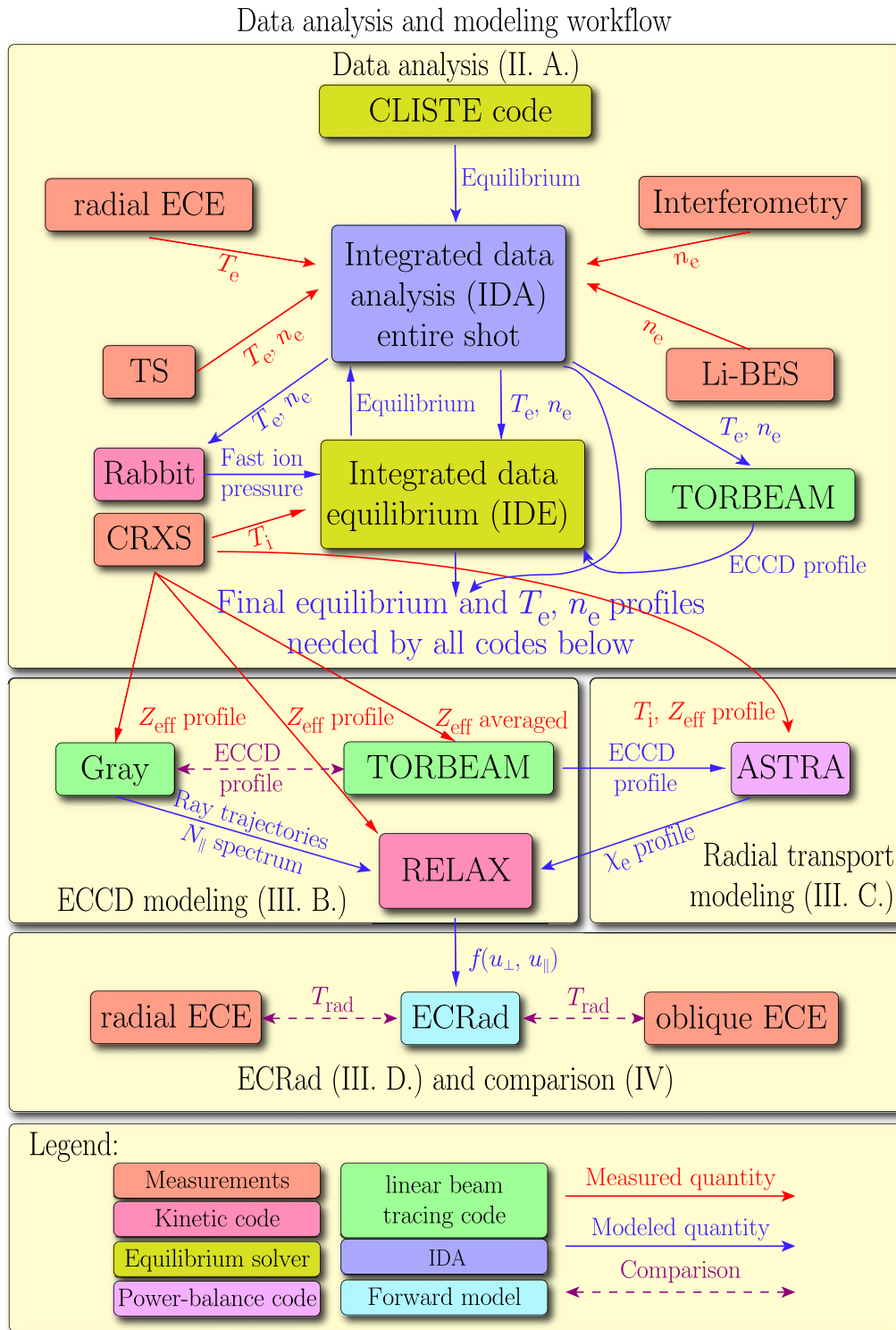


**Figure 3.** Flowchart illustrating the data analysis and modeling in this paper. The top layer is the data analysis of the  $T_e$  and  $n_e$  profiles and the magnetic equilibrium. The next level is the ECCD and radial transport modeling. The final layer is the computation of the synthetic ECE measurements.

(e) The radiation reaction force [36].

With the exception of collisions, all of these effects can be toggled on and off, which allows their importance to be assessed.

RELAX does not have an internal ray tracer; hence we rely on the beam tracing code Gray [30] for this purpose. In the previous step, TORBEAM was used for ECRH beam tracing because TORBEAM is tightly integrated with the ASDEX Upgrade infrastructure. However, Gray is preferable for the



interfacing with RELAX because the RELAX calculations were performed on the EUROFUSION WPCD gateway, and Gray provides its output as a Consistent Physical Object [48] that can be loaded by RELAX. The integrity of the data transfer from GRAY and RELAX was verified using scenarios in which the electron cyclotron damping is linear with respect to the power.

Gray discretizes the beam into concentrically arranged rays, and in the calculations discussed here, 7 radial times 25 poloidal rays summing up to  $1 + 6 \times 25 = 151$  total rays are considered. The rays are shown in figure 2, and the color indicates the power remaining in the individual ray. Since beam tracing codes are used, diffraction is taken into account, but beam broadening due to turbulent  $n_e$  fluctuations is neglected, the importance of which will be the subject of a future paper.

The loop voltage  $U_{\text{loop}}$  responsible for the parallel electric field is assumed to be radially constant. Its value is calculated by solving  $I_{p,\text{target}} = I_p(U_{\text{loop}})$ , where  $I_{p,\text{target}}$  is the measured plasma current and the profile  $I_p = I_p(U_{\text{loop}})$  is constructed through a spline interpolation of the steady-state current predicted by RELAX with input  $U_{\text{loop}} = j\Delta U_{\text{loop}}$ ,  $j \in \{0, 1, \dots, 5\}$ , and  $\Delta U_{\text{loop}} = 0.2 \text{ V}$ . Since RELAX cannot compute the bootstrap current,  $I_{p,\text{target}}$  is the experimentally measured current minus the bootstrap current provided by the IDE [44] code. Radial diffusion is neglected when computing the loop voltage, since its effect on the plasma current is of the order of few kA, which is negligible. For  $t = 3.84 \text{ s}$ , a loop voltage of  $0.36 \text{ V}$  is computed, which is reasonably close to the measured value of  $0.44 \text{ V}$ .

To ensure that the distribution function predicted by RELAX has been iterated sufficiently to have reached steady-state,  $T_{\text{rad}}$  is computed via *ECRad* for every 500th intermediate distribution until

$$\sqrt{\sum_{i=1}^{N_{\text{ch}}} (T_{\text{rad},i}(n) - T_{\text{rad},i}(n-1))^2} < N_{\text{ch}} \text{ eV}, \quad (1)$$

where the radiometer channel number is  $i$ ,  $N_{\text{ch}}$  is the total amount of forward-modeled ECE channels, including the radial ECE + the two oblique ECE systems, and  $n$  is the count of RELAX iterations.

Figure 4(a) compares the power deposition profile computed by Gray, TORBEAM, and RELAX, considering only collisions and ECRH. TORBEAM and Gray agree reasonably well, and the quasi-linear power deposition profile computed by RELAX is very similar to the two linear counterparts. Near the magnetic axis, TORBEAM predicts a slightly different power deposition profile, which is most likely due to the way TORBEAM calculates the plasma volume. Figure 4(b) compares the corresponding current densities. Here Gray and TORBEAM disagree quite strongly for unknown reasons that are still under investigation. However, since the distribution functions computed by RELAX are independent of the two linear calculations, this is not an issue for the physics investigated in this paper. RELAX shows the largest driven current. Since the TORBEAM and RELAX driven current profiles match in

case of a linear ECCD response at  $1 \text{ kW}$  of power (not depicted), it is safe to conclude that the excess current predicted by RELAX in figure 4(b) is due to quasi-linear effects. The predicted total driven currents are  $-29 \text{ kA}$  for Gray,  $-38 \text{ kA}$  for TORBEAM, and  $-47 \text{ kA}$  for RELAX.

Figure 4(c) shows the  $T_e$  and  $n_e$  profiles computed by the IDA code, which are supplied to RELAX. It also shows the  $n_e$  and the ' $T_e$ ' computed from the zeroth and 2nd moment of the non-thermal RELAX distribution function. The density profile remains unchanged because it is forced to be fixed for all RELAX calculations shown in this paper to improve numerical stability. At the peak of the deposition profile, the ' $T_e$ ' as given by the second moment of the RELAX distribution, is slightly elevated with respect to the initial temperature. This occurs in the same region where the TORBEAM and RELAX driven current profiles deviate from each other, which confirms that the ECCD response is non-linear in this region.

### 3.3. Radial transport modeling

Figure 5 shows the electron heat diffusion profile as derived from the power balance by ASTRA [49]. This profile cannot be used directly in RELAX due to numerical difficulties arising in RELAX for the very large heat diffusivities near the plasma edge. This problem can be avoided by disregarding radial transport in this region completely, which the oblique ECE measurements are anyway insensitive to. Hence, the simplified  $\chi_e$  profile as depicted in figure 5(a) is considered in the RELAX computations.

Three different models for the momentum space dependence are considered in this paper, here termed models A, B, and C. For model A, the radial diffusion coefficient is momentum independent and for

$$\text{Model B: } D_{\text{Model B}}(\rho_{\text{pol}}, u) = \chi_{e,\text{simpl}}^*(\rho_{\text{pol}}) \frac{u^2}{u_{\text{th},0}^2} \quad (2)$$

and

$$\text{Model C: } D_{\text{Model C}}(\rho_{\text{pol}}, u) = \chi_{e,\text{simpl}}^*(\rho_{\text{pol}}) \exp\left(-\frac{u^2}{4u_{\text{th},0}^2}\right) \quad (3)$$

with  $u = \frac{p}{m_{e,0}c_0}$  the total dimensionless momentum, whereas  $p$  is the electron momentum,  $m_{e,0}$  the electron rest mass,  $c_0$  the speed of light in vacuum, and

$$\rho_{\text{pol}} := \sqrt{\frac{\Psi_{\text{pol}} - \Psi_{\text{pol,ax}}}{\Psi_{\text{pol,sep}} - \Psi_{\text{pol,ax}}}}$$

where  $\Psi_{\text{ax}}$  and  $\Psi_{\text{sep}}$  are the poloidal flux at the magnetic axis and the separatrix, respectively. The thermal momentum computed for  $T_e$  at the magnetic axis is denoted as  $u_{\text{th},0}$ , and it is approximately  $0.09$  for the discussed discharge and time point. While it might be more meaningful to use the local thermal velocity as reference, this would make the normalization discussed below much more complicated due to the radial

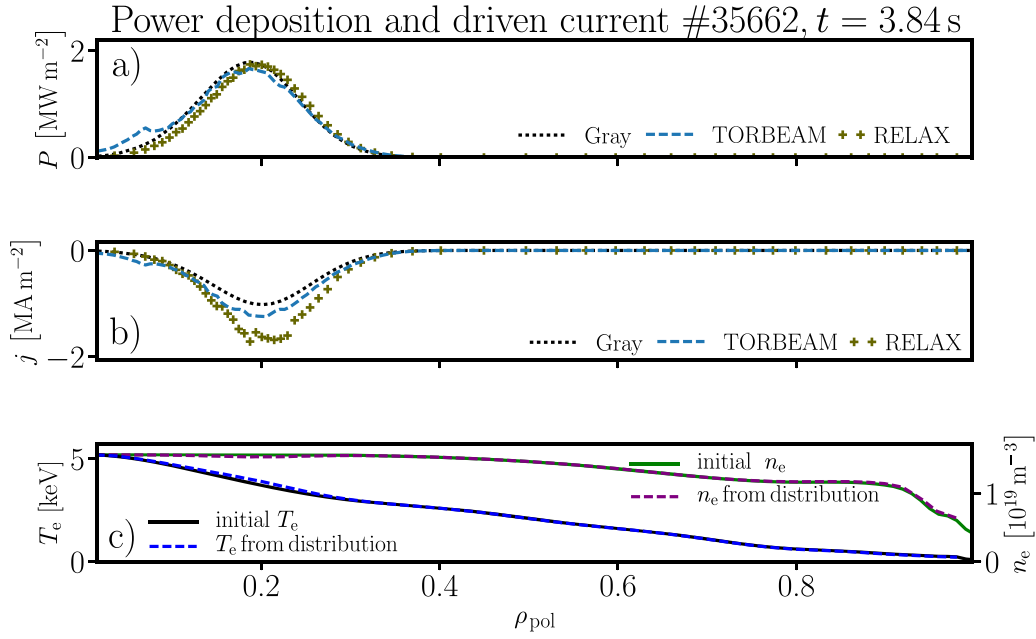


**Figure 4.** (a) Comparison of the power deposition profiles computed by Gray, TORBEAM, and RELAX for the case of only quasi-linear electron cyclotron diffusion and collisions. (b) as in (a) but for the current density profile. (c) Comparison of the initial  $n_e$  and  $T_e$  with their respective counterparts computed from the zeroth and second moment of the RELAX distribution function.

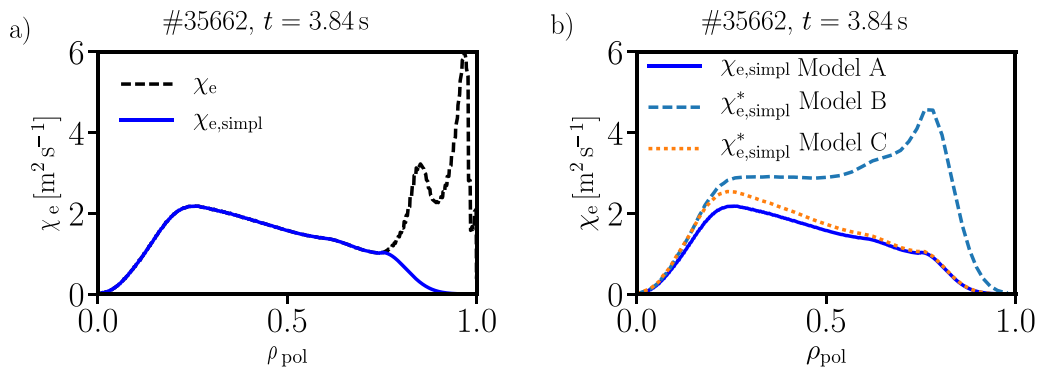


**Figure 5.** (a) Electron heat diffusivity profile as derived from the power balance by ASTRA. Due to numerical issues in RELAX occurring with the original  $\chi_e$  profile, the simplified version  $\chi_{e,\text{simpl}}$  is considered in the RELAX calculations. (b) Comparison of  $\chi_{e,\text{simpl}}$  with its renormalized counterparts  $\chi_{e,\text{simpl}}^*$  for model B and C.

dependence of  $u_{\text{th}}$ . The normalized  $\chi_{e,\text{simpl}}^*(\rho_{\text{pol}})$  is obtained by dividing  $\chi_{e,\text{simpl}}(\rho_{\text{pol}})$  by

$$\text{Model B: } \mathcal{N}_{\text{B}}(\rho_{\text{pol}}) = \int_{-\infty}^{\infty} \int_{-\infty}^{\infty} \frac{u_{\perp}^2 + u_{\parallel}^2}{u_{\text{th},0}^2} \hat{f}(\rho_{\text{pol}}, u_{\perp}, u_{\parallel}) u_{\perp} du_{\parallel} du_{\perp} \quad (4)$$

$$\text{Model C: } \mathcal{N}_{\text{C}}(\rho_{\text{pol}}) = \int_{-\infty}^{\infty} \int_{-\infty}^{\infty} \exp\left(-\frac{u_{\perp}^2 + u_{\parallel}^2}{4u_{\text{th},0}^2}\right) \hat{f}(\rho_{\text{pol}}, u_{\perp}, u_{\parallel}) u_{\perp} du_{\parallel} du_{\perp} \quad (5)$$

with  $u_{\parallel}$  and  $u_{\perp}$  the parallel and perpendicular momentum with respect to the magnetic field, and  $\hat{f}$  the electron momentum

distribution function normalized to unity. This renormalization ensures that the effective, momentum space integrated diffusion coefficient is comparable among all three models at each radial point. Since model A carries no momentum dependence, and the distribution function is normalized to unity,  $\chi_{e,\text{simpl}}$  and  $\chi_{e,\text{simpl}}^*$  are identical for model A. Please see appendix B for a derivation of the normalization procedure.

The main purpose of the differentiation between models B and C is to determine whether fast or slow electrons are responsible for the majority of the radial heat-transport. Gyrokinetic calculations for off-axis positions in ITER show that electrostatic turbulence is dominant, and slow, trapped electrons are responsible for the majority of the radial transport [50]. Qualitatively, the same behavior was also seen in gyrokinetic calculations of TCV plasmas with central ECCD, which is similar to the scenario discussed here [51]. Hence, it is expected that model C should yield the best agreement with

the experiment. If, however, magnetic turbulence is dominant in the experiment, then the radial transport increases linearly with electron velocity and one would expect model B to produce the best agreement with the measurements [52].

### 3.4. ECRad

The *ECRad* [28] code is used to compute synthetic ECE spectra. It is a ray tracing code that also solves the radiation transport equation, taking into account a fully relativistic absorption coefficient and emissivity suitable for non-thermal plasmas. In the calculations, the effect of finite bandwidth is disregarded, but the finite width of the volume of sight is modeled by a rectangular bundle of  $5 \times 5$  rays. Aside from this, the configuration is the same as in references [28, 36].

## 4. Comparison of ECE measurements with modeled spectra

In the following section, all ECE measurements of #35662 are compared to their synthetic counterparts. The time point  $t = 3.84$  s is chosen because the plasma is stationary around it for 10 ms, which is longer than the approximate time required to achieve convergence in RELAX. The only non-stationary feature is a  $1/1$  (where  $m/n$  represent the poloidal and toroidal mode number) ideal magnetohydrodynamic (MHD) kink mode, rotating in the plasma center with a frequency of about 2.6 kHz. Its possible effects on the measurements and the modeling are addressed in the discussion at the end of the paper (see section 6).

### 4.1. Conventional, radial ECE

Before addressing the more important oblique ECE measurements, it is useful to discuss the radial ECE measurements that deliver the  $T_e$  information for the truncated collision operator in RELAX and the initial distribution function.

Figure 6 compares the measured ECE spectrum against two synthetic sets of  $T_{\text{rad}}$ . The synthetic spectrum depicted with purple squares is derived from a thermal distribution function, while the distribution computed by RELAX is considered in ECRad for the data visualized with blue upside down triangles. Radial diffusion is neglected in the RELAX calculation. The  $T_e$  profile considered for the thermal  $T_{\text{rad}}$  is depicted by a black line, and the upper and lower uncertainty bands, as estimated by the IDA, are shown via the dashed purple lines.

Generally, the deviations between the two synthetic ECE spectra are negligible. Most importantly, the distribution function computed by RELAX results in  $T_{\text{rad}}$ , which are consistent with the ECE measurements in the plasma core. This means that the modeling is self-consistent, and that the  $T_e$  profile considered in the truncated collision operator is realistic.

For cold resonance position  $\rho_{\text{pol, res, cold}} > 1.0$ , there are deviations between the two sets of  $T_{\text{rad}}$  in figure 6. However, the optical depth of these channels is below 0.5, and *ECRad* is unable to model these ECE measurements properly due to its limited wall reflection model. Without a more suitable wall

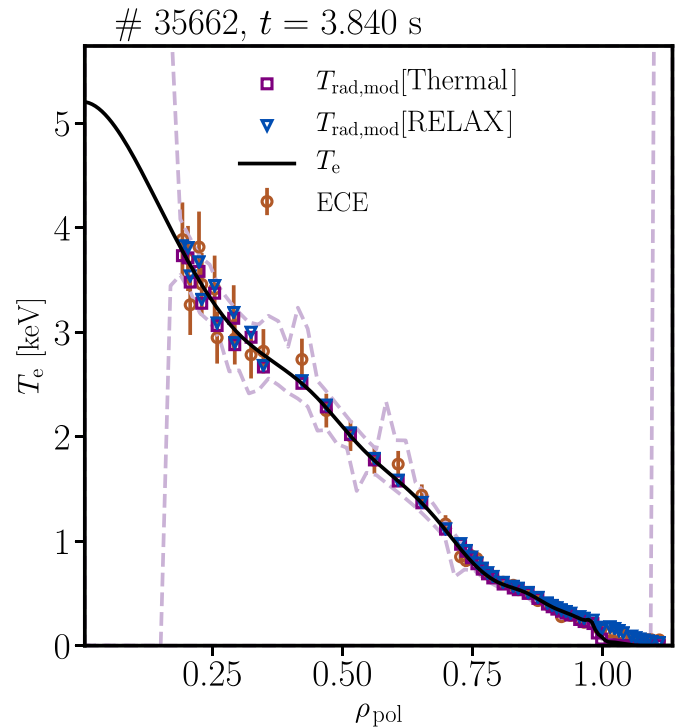


**Figure 6.** Comparison of  $T_{\text{rad}}$  measured with the radial ECE with two sets of synthetic data, i.e. based on a thermal plasma and derived from a RELAX distribution in the absence of radial diffusion. The figure also shows the  $T_e$  profile derived with IDA (black solid line) and its corresponding upper and lower error bands (dashed purple lines).

reflection model, e.g. the one proposed in reference [53], these measurements cannot be interpreted quantitatively.

### 4.2. Oblique ECE measurements

The VOS of the oblique ECE is chosen such that it measures the distribution function directly at the deposition site of the ECRH (see also section 5). The oblique ECE measurements are compared to five sets of synthetic spectra assuming:

- (a) Thermally distributed electrons.
- (b) The distribution function computed by RELAX in the absence of radial diffusion.
- (c)–(e) The distribution functions computed by RELAX for the radial diffusion models A, B, and C.

This means that the electron cyclotron diffusion, collisions, the loop voltage, and the radiation reaction force are included in all considered RELAX calculations. Notably, the effect of the parallel electric field is non-negligible, as it reduces the forward-modeled radiation temperatures by 5–10% when added to calculations with collisions and electron cyclotron diffusion. The radiation reaction force [36], however, results in negligible changes in  $T_{\text{rad}}$  when added into the mix.

Figure 7 compares the measured radiation temperatures of the ctr-ECE (reminder: this is the ‘CTA’ array) with the five sets of synthetic data computed with ECRad. As the



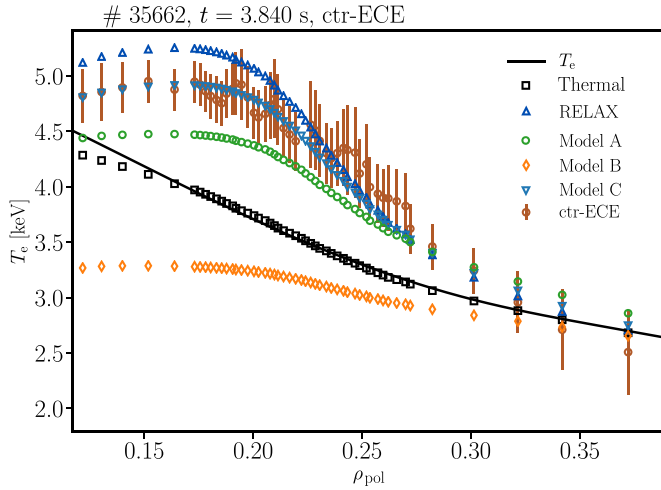


**Figure 7.** Comparison of  $T_{\text{rad}}$  measured with the ctr-viewing oblique ECE primarily sensitive to counter-streaming electrons with five sets of synthetic data, i.e. thermal plasma, RELAX without radial diffusion (i.e. RELAX), and RELAX with radial diffusion model A–C (i.e. Model A, B, and C).

name suggests, this diagnostic is primarily sensitive to ctr-streaming electrons, which are directly affected by the ECCD. A thermal plasma is assumed for the data depicted by the black squares, while a RELAX distribution function in the absence of radial diffusion is assumed for the dark blue triangles. Furthermore, figure 7 shows the synthetic data for the three different radial diffusion models: A (light blue upside down triangles), B (orange diamonds), and C (green circles). The various  $T_{\text{rad}}$  are mapped to the maximum of the birthplace distribution of observed intensity, i.e. ‘warm’ resonance positions  $\rho_{\text{pol, res, warm}}$ . To make the  $\rho_{\text{pol, res, warm}}$ -positions uniform for all  $T_{\text{rad}}$ , the birthplace distributions resulting from the non-thermal distribution function in the absence of radial diffusion are used for all ‘warm’ resonance positions. Figure 8 shows the same as figure 7 but for the co-ECE (reminder: this is the ‘CTC’ array), which is primarily sensitive to co-streaming electrons that are only indirectly affected by the ECCD through collisions.

In figure 7, the agreement between measurements and the  $T_{\text{rad}}$  based on RELAX with model C for radial diffusion is good at the plasma core, and only small discrepancies arise for  $0.2 < \rho_{\text{pol, res, warm}} < 0.27$ . For the co-ECE, the two innermost channels are not matched by model C, but otherwise the agreement is excellent. The radial diffusion models A and B result in  $T_{\text{rad}}$  that only agree for the measurements that are very close to thermal level. Generally, it appears that model A smears out the non-thermal features of the distribution function too much as it starts overpredicting the measurements at large  $\rho_{\text{pol}}$ . Most importantly, the large difference in the  $T_{\text{rad}}$  predicted by models A, B, and C shows that, with oblique ECE it is possible, to determine which energy domain is responsible for the radial transport. In this case, model C shows the best agreement, which is expected given gyrokinetic simulations for ITER [50].

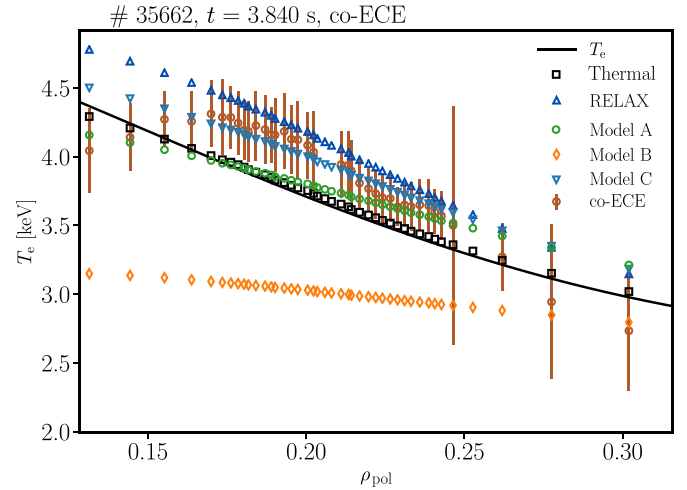


**Figure 8.** Same as figure 7 but for the co-ECE.

When examined closely, the ctr-ECE measurements between  $0.18 < \rho_{\text{pol, res, warm}} < 0.27$  in figure 7 show a slight sinusoidal structure, which cannot be seen in any of the synthetic  $T_{\text{rad}}$  and neither in the co-ECE measurements. Given the comparatively large error bars, it is hard to tell whether this is an error in the cross-calibration or due to a feature in the distribution function that is not captured by the distribution functions computed by RELAX. It is noteworthy that the cross calibration is unlikely to yield systematic errors with this shape, as the  $T_e$  profile should be reasonably smooth at these length scales. Without further experiments verifying the existence of these structures, an interpretation is not feasible at this point.

## 5. Sensitivity of the ECE measurements in phase space

The main novel feature of this paper is the utilization of oblique ECE for the validation of the quasi-linear theory for ECCD. The main merit of oblique ECE diagnostics is the phase space region they are able to resolve. In this section, the phase-space sensitivity of the radial and oblique ECE measurements presented in the previous section is discussed.

### 5.1. Birthplace distribution of observed intensity in phase space

The main tool for this discussion is the birthplace distribution function of observed intensity [28, 37, 38]. Ordinarily, this distribution is constructed as a function of a single, radial coordinate, but it can be extended to phase space. The basic, one-dimensional birthplace distribution of observed intensity  $D_\omega(s)$  at frequency  $\omega$  is given as a function of the arc-length  $s$  [37] by

$$D_\omega(s) := \frac{j_\omega(s)\mathcal{T}_\omega(s)}{I_\omega(s_{\text{obs}})}, \quad (6)$$

where  $j_\omega(s)$  is the emissivity,  $I_\omega(s_{\text{obs}})$  is the intensity obtained by solving the radiation transport equation, and lastly,  $\mathcal{T}_\omega(s)$

is the transmittance of the plasma slab between point  $s$  and the observation point  $s_{\text{obs}}$ . It is defined as

$$\mathcal{T}_\omega(s) := \exp\left(-\int_s^{s_{\text{ant}}} \alpha_\omega(s') ds'\right), \quad (7)$$

where  $s_{\text{ant}}$  is the arc-length at the antenna position and  $\alpha_\omega$  is the absorption coefficient as given by reference [54]. In the case of a calculation considering a finite volume of sight, as is done here, it is best to bin the contribution of the individual rays to a  $\rho_{\text{pol}}$ -axis.

To extend the birthplace distribution to phase space, the integral in the dimensionless parallel momentum  $u_{\parallel}$  in the emissivity is omitted [28, 54]

$$D_\omega^*(s, u_{\parallel}) := \frac{\mathcal{T}_\omega(s)}{I_\omega} \frac{\omega_{p,0}^2 \omega}{2\pi c_0^3} \int \left( \frac{n}{\bar{\omega} N_{\perp}} \right)^2 \left| \left( e_x + \frac{\bar{\omega} N_{\perp}}{n} u_{\parallel} e_z \right) J_n(b) - \frac{ib}{n} J'_n(b) e_y \right|^2 \times \hat{f}(s, u_{\perp}, u_{\parallel}) \delta\left(\gamma - u_{\parallel} N_{\parallel} - \frac{n}{\bar{\omega}}\right) \frac{u_{\perp}}{\gamma} du_{\perp}. \quad (8)$$

For details on the notation, please see reference [28], and note the electron momentum distribution function normalized to unity is expressed as  $\hat{f}$ , while it is denoted as just  $f$  in reference [28]. This extension is only valid for a single ray, and in the following, only the central ray is discussed.

Analogously, a mock-up of the phase-space-resolved power deposition profile can be obtained by replacing the emissivity with the absorption coefficient in equation (6) and removing the normalization  $I_\omega$ . It is noteworthy that this function is not really a power deposition profile anymore because it lacks the dependency of the flux surface volume that the power deposition profile holds. Instead, this construct is a function defined for a singular ray of the ECRH beam, e.g. the central ray in the following, and will be denoted as  $dP_{\text{ECRH}}^*/ds$  in the following.

## 5.2. Power deposition in phase space

Illustrations of the resonance of an infinitely thin ECRH beam in momentum space have been in use for quite some time now for understanding ECCD (see e.g. reference [55]). With the following illustration of the three-dimensional mock-up of the power deposition profile, we also intend to capture the spatial dependence of the resonance in momentum space.

In figure 9(a), the power deposition profile as computed by Gray and RELAX are shown. For reference,  $T_e$  is also indicated. Figure 9(b) illustrates the resonance in momentum space of the central ray. The figure also shows the iso-contours of the distribution function computed by RELAX for the radial location indicated by the middle vertical line in (a), i.e.  $\rho_{\text{pol}} = 0.16$ . While the contours are circular at small  $u$  indicating a thermal distribution, significant anisotropy arises for larger  $u$ .

The color-coded semicircular lines show where the resonance condition is fulfilled at the three radial locations indicated by the dashed vertical lines in figure 9(a). The innermost semicircle in 9(b) corresponds to the outermost radial location. The radius of the semicircle increases with decreasing  $\rho_{\text{pol}}$ . The

resonances are color-coded, where yellow corresponds to a large amount of deposited power and pink to negligible power deposition. Most of the power is deposited at low momenta.

Note that figure 9(b) only illustrates the behavior of the central ray of the ECRH beam. In reality, the resonance is broadened in momentum space due to the finite width of the parallel wave number  $\vec{k}_{\parallel}$  spectrum and the finite spatial extent of the ECRH beam. Here, it is useful to point out that quasi-optical codes like Gray underestimate the  $\vec{k}$ -spectrum at the beam focus [56]. To compensate for this, RELAX slightly broadens the  $\vec{k}_{\parallel}$ -spectrum internally. The benefit of using a quasi-optical code like Gray is of course that spatial broadening of the beam due to diffraction is correctly included.

The resonance of the ECRH beam defines our region of interest in phase space in which the distribution function has to be measured to validate the quasi-linear theory for ECRH damping. In the following section, it is demonstrated that this region is inaccessible to conventional radial ECE. That it is accessible with oblique ECE is shown in section 5.4.

## 5.3. Phase-space sensitivity of radial ECE diagnostics

Figure 10(a) shows a zoomed-in view of figure 9(a) and with a birthplace distribution added, representing the sensitivity of the radial ECE channel with  $\rho_{\text{pol, res, cold}} = 0.17$ . In figure 10(b), the corresponding resonance lines for the radial ECE diagnostic were added. As indicated by the green coloration of the resonance lines, the diagnostic is mainly sensitive to slow, trapped electrons. In fact, there is no direct overlap between the phase space region where the ECRH deposits significant amounts of power and the one where the diagnostic is actually sensitive.

For  $u < 0.15$ , RELAX predicts what is essentially a thermal distribution function. As figure 10(b) shows this channel is only sensitive to electrons with  $u < 0.15$ , in the plasma core. Therefore, it is unsurprising that the forward-modeled  $T_{\text{rad}}$  for this channel is identical to that expected from a thermal distribution. Furthermore, the  $T_e$  profile inferred from the radial ECE measurements is suitable for the truncated collision operator, as only highly collisional electrons contribute to the measurement. This can change at very large  $T_e$  where the strongly down-shifted emission from relativistic electrons can contribute through higher harmonics. This requires a population of electrons with  $u > 1.0$ . This momentum corresponds to more than twelve times the thermal momentum in the plasma core of #35 662. In addition, at larger  $T_e$ , the contributing electrons will have larger momenta and, consequentially, lower collisionality, making plasma core measurements with radial ECE more prone to non-Maxwellian tails in the electron momentum distribution.

One of the most prominent features of non-thermal ECE is a large  $T_{\text{rad}}$  observed at frequencies that have no cold resonance position in the plasma. However, such measurements are not probing the phase space region where the majority of the ECRH power is absorbed. While the resonance lines of the ECE and ECRH might still intersect, the majority of the ECRH power absorption occurs at comparatively low momenta, whereas the ECE stems from a few, very highly

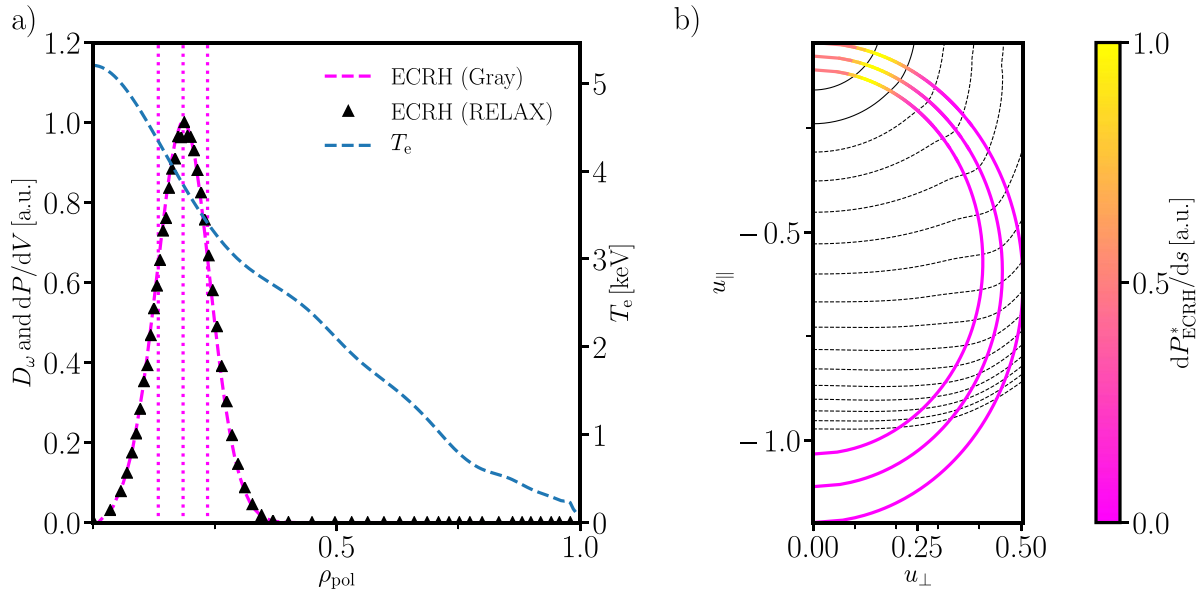


**Figure 9.** (a) Power deposition profiles computed by Gray and RELAX and the  $T_e$  profile. The contours in (b) represent the distribution function computed by RELAX at the radial location marked by the middle vertical line in (a). The color-coded semi-circles indicate where the ECRH power is absorbed in phase space at the three radial locations marked by the vertical lines in (a). The outermost semicircle in (b) corresponds to the innermost radial location in (a), the middle to the middle radial location, and the innermost to the outermost radial location.

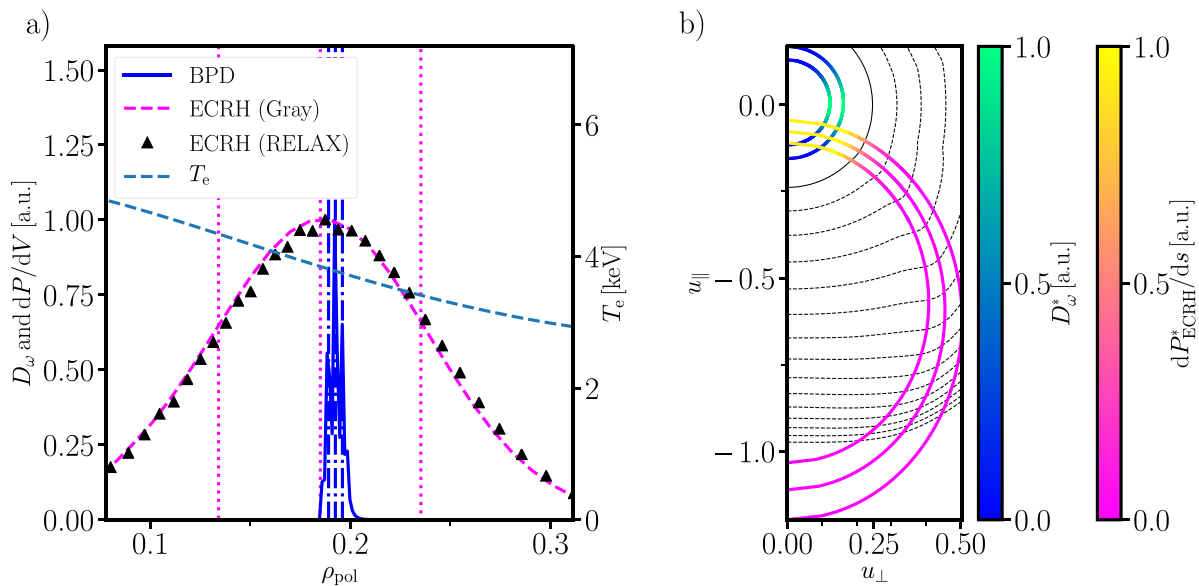


**Figure 10.** (a) Zoomed-in view of figure 9(a) with the addition of the birthplace distribution function (BPD) of a radial ECE channel with the cold resonance at  $\rho_{\text{pol, res, cold}} = 0.17$ . Figure (b) shows the same as figure 9(b), but the resonance lines of this radial ECE channel were added. The radial locations for these resonance lines are indicated by blue vertical lines in (a). Since the birthplace distribution is extremely narrow, two of the resonance lines overlap and, hence, only two are visible.

energetic electrons. This is demonstrated in figure 11, which shows the same as figure 10, but for a radial ECE channel with  $\rho_{\text{pol, res, cold}} = 0.96$ . This particular channel is chosen because its optical depth is approximately one, which means that the measurement is not yet completely dominated by wall reflections, but still sensitive to non-thermal, down-shifted emission originating from the plasma core.

The birthplace distribution in figure 11(a) was multiplied by 100 to make the core contributions more easily visible. It

shows a large peak near the cold resonance near the plasma edge, but also a small broad region of observed emission near the plasma core. The corresponding resonance lines in (b) show that this emission stems from the highly energetic electrons at the intersection of the ECRH and ECE resonance lines. While the distribution function is highly non-thermal in this region of momentum space, the vast majority of the power deposition occurs at lower momenta, which are inaccessible for the radial ECE.

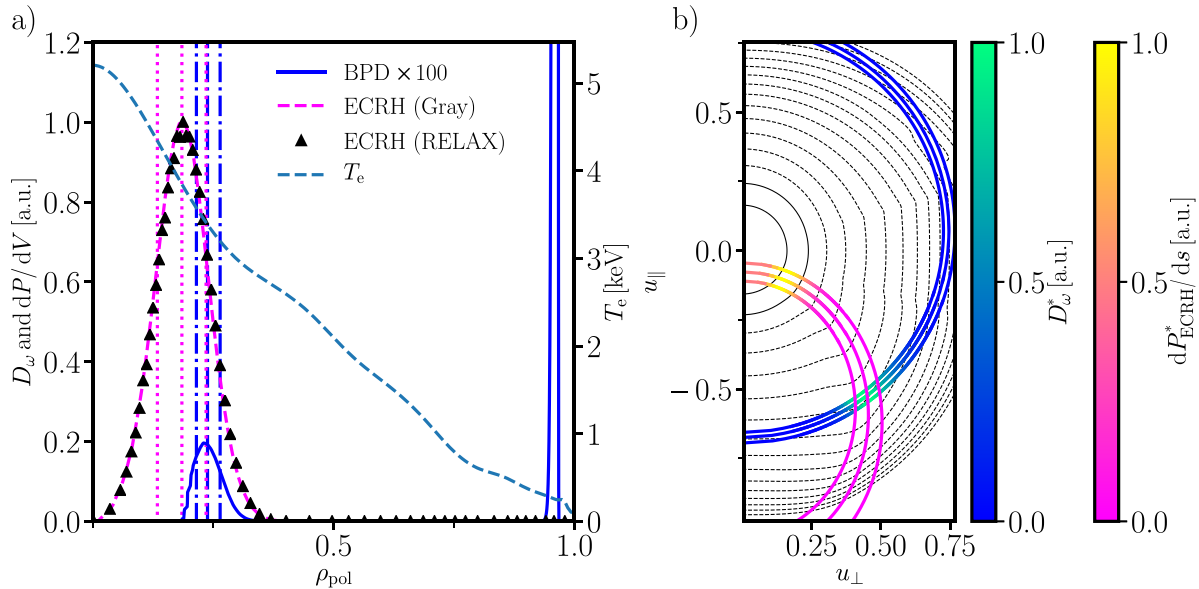


**Figure 11.** As in figure 10 but for a radial ECE channel with the cold resonance at  $\rho_{\text{pol, res, cold}} = 0.96$ .

#### 5.4. Phase-space sensitivity of oblique ECE diagnostics

Figure 12 shows the same as figure 11, but for a channel of the ctr-ECE. As can be seen in (a), the power deposition profile of the ECRH and the birthplace distribution of the oblique ECE channel overlap nearly completely. The only exception is the very core, at which there is still non-zero power deposition while the birthplace distribution is vanishingly small. Since the poloidal alignment between oblique ECE and ECRH is not quite perfect, the central ray of the oblique ECE is slightly further away from the magnetic axis than the central ray of the ECRH (cf. Figure 2(a)). In fact, the measured frequency of this particular channel is 108.7 GHz, while the gyrotron frequency is 105 GHz.

Nevertheless, the radial match between oblique ECE sensitivity and ECRH power deposition is good. As with the previous figures, figure 12(b) compares the resonances of the ECRH and the ctr-ECE in momentum space. First and foremost, the coloration of the respective ECE and ECRH resonance lines indicates that the power is deposited in the region where the oblique ECE is sensitive. Hence, in this case, the oblique ECE probes the electrons subject to the quasi-linear electron cyclotron diffusion. This particular channel, with a warm resonance position of  $\rho_{\text{pol, res, warm}} = 0.15$ , belongs to the group of channels where the agreement between diagnostic and synthetic data is excellent (cf. figure 7) in case of radial diffusion model C.

When compared in detail, the resonance lines of ECRH and ECE do not match up perfectly. The discrepancy arises because the central frequency of this channel differs from frequencies of the gyrotron. Despite the frequency mismatch, this channel has the best radial overlap with the power deposition profile.

Figure 13 shows the same as figure 12 but for the channel with the warm resonance at  $\rho_{\text{pol, res, warm}} = 0.25$ . This channel measures the ECE at 104.5 GHz, which is much closer to

the gyrotron frequency than the previously discussed channel. Nevertheless, the radial match between birthplace distribution and power deposition profile is worse for this channel as shown in figure 13(a) due to the slight mismatch of poloidal launch/viewing angle.

The toroidal observation angle of the co-ECE has the opposite sign with respect to the ctr-ECE. In momentum space, that causes the resonance lines to be mirrored around the  $u_\parallel = 0$  axis. Figure 14 compares the birthplace distribution for a channel of the co-ECE with the power deposition profile  $\rho_{\text{pol, res, warm}} = 0.16$ , and (b) shows its resonance lines. The co-ECE does not deliver data on the distribution function in the region of phase space where the ECRH is absorbed, but it still delivers valuable information. The deformations of the distribution functions caused by the ECCD for  $u_\parallel < 0$  give rise to the driven current. Some of this current is, however, compensated by similar deformations appearing for  $u_\parallel > 0$  due to pitch angle scattering. This effectively reduces the current drive efficiency, and the magnitude of this effect can be assessed with the co-ECE.

#### 5.5. Including the finite width of the ECRH beam and the VOS

So far only the central ray of the ECRH beam and the VOS of the oblique ECE were considered for the momentum space plots. To include the finite width of the beam and the VOS, the 3D power deposition and birthplace distribution profiles of the individual rays need to be binned to a universal momentum space grid. This can be done by integration in two steps. First, the resonance line at each radial point needs to be binned to the momentum space grid. This is accomplished by finding the intersections between the resonance line and the grid cells. Then, the path integral of the birthplace distribution from one border of the cell to the other is added to the value of the cell.

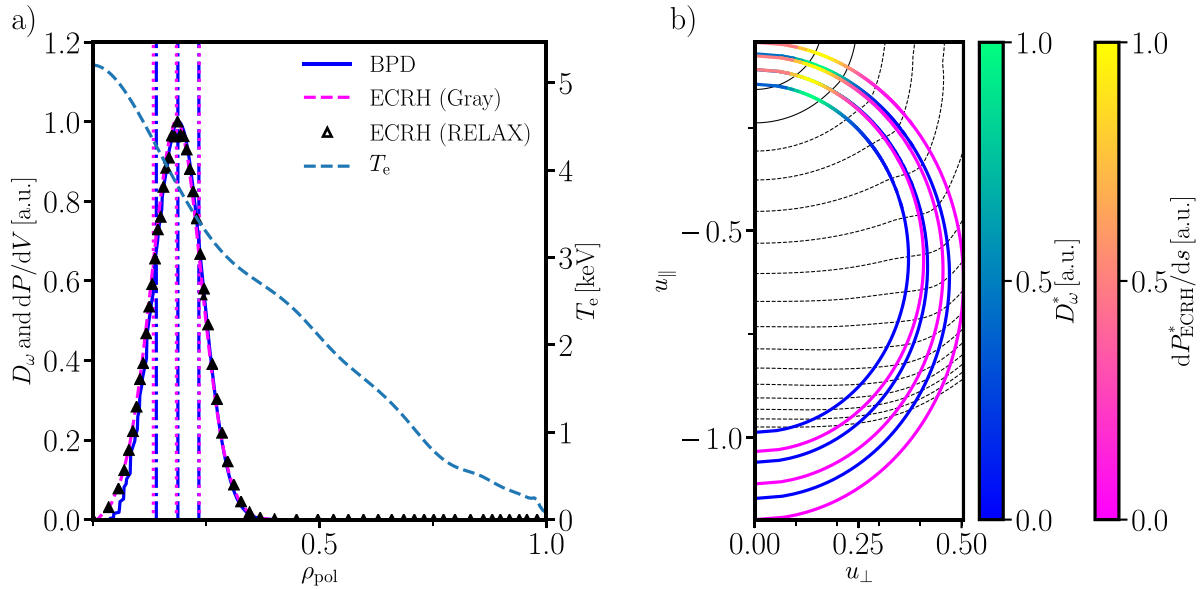


**Figure 12.** As figure 11 but for an oblique ECE channel of the ctr-ECE with the warm resonance at  $\rho_{\text{pol, res, warm}} = 0.15$ .

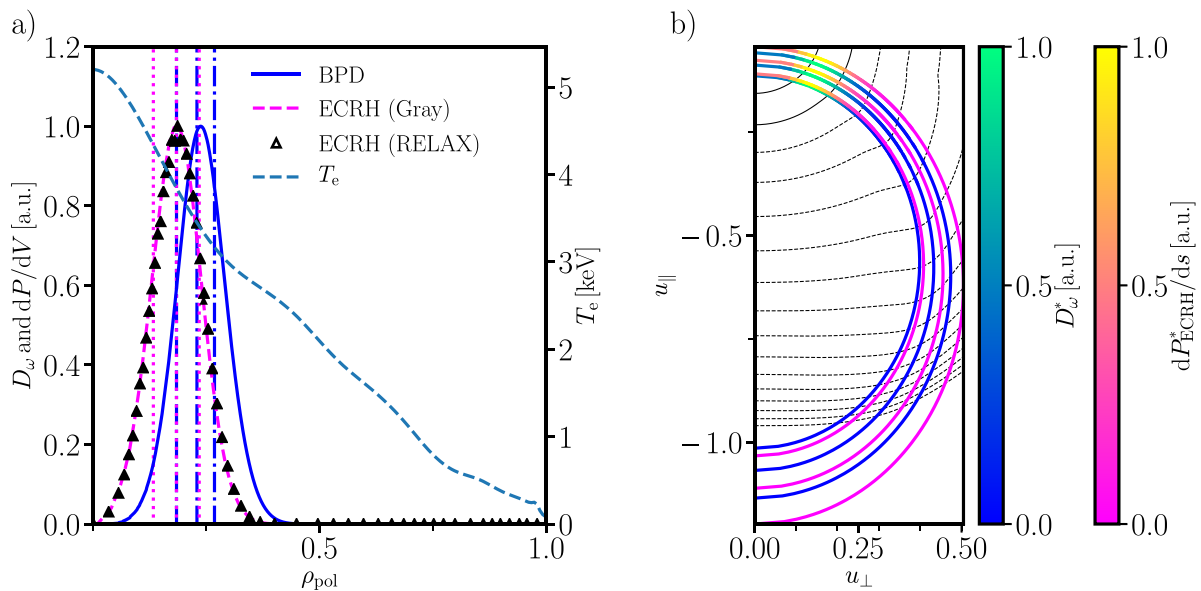


**Figure 13.** As figure 12 but for an oblique ECE channel with a warm resonance position slightly further outside than in figure 12 at  $\rho_{\text{pol, res, warm}} = 0.25$ .

The radial dependency is removed by repeating this process for each radial point and weighing the individual contributions of the radial point with the value of 1D power deposition or birthplace distribution function, respectively.

In figure 15, the resulting, binned 3D birthplace distribution function of the two oblique ECE diagnostics is compared to the corresponding power deposition profile of the gyrotron. The yellow to purple contour lines indicate the sensitivity of the oblique ECE diagnostics, while the green contour surfaces show where the gyrotron deposits its power in momentum space. The contours marked with ctr-ECE are for the same channel as in figure 12, and for the co-ECE, it is the same as in figure 14. The plot confirms that the ctr-ECE measures the

distribution function in the region of momentum space where the ECRH deposits its power.

### 5.6. Oblique ECE as a diagnostic for the plasma current

Given that oblique ECE can be set up to measure either co- or counter streaming electrons, one could come to the conclusion that it might be able to deliver a measurement for the local plasma current. Unfortunately, for #35 662, the sensitivity of the oblique ECE is not in the right region of momentum space to allow this. This is illustrated in figure 16. The blue-red colored contour surfaces indicate  $(f - f_0)\beta_\parallel$  with  $f$  the electron momentum distribution function computed by RELAX,



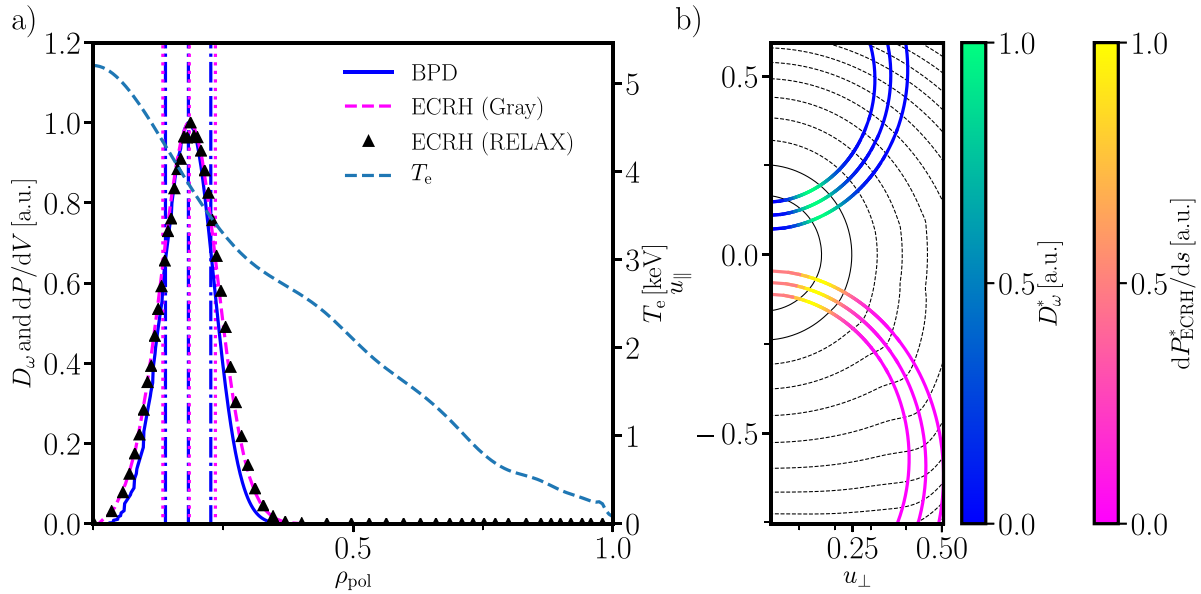


**Figure 14.** As figure 12 but for an oblique ECE channel of the co-ECE with a warm resonance position at  $\rho_{\text{pol, res, warm}} = 0.16$ .

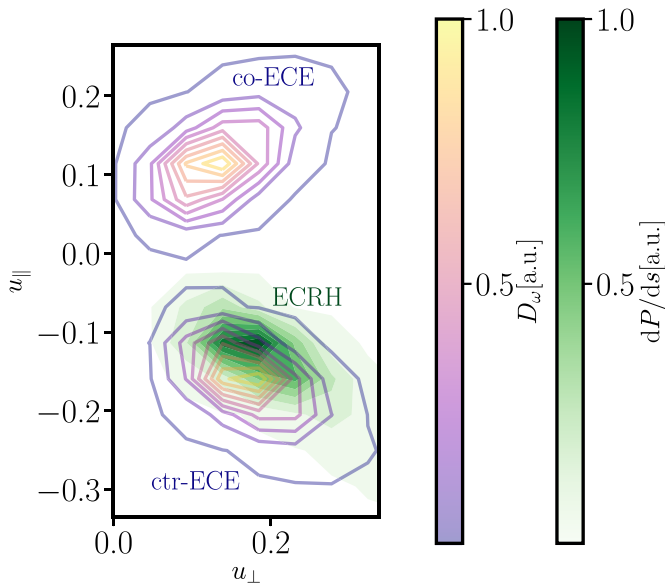


**Figure 15.** Comparison of the momentum-space sensitivity (yellow to purple contour lines) of the ctr- and co-ECE with the regions in momentum where the ECRH deposits its power (green contour surfaces).

$f_0$  the thermal distribution as given by the  $T_e$  profile, and  $\beta_{\parallel}$  the parallel electron velocity normalized to the speed of light. In figure 16(a) only collisions, and ECCD are considered for  $f$ , while (b) also includes the loop voltage, the radiation reaction force, and radial diffusion model C in the RELAX calculation.

To obtain the contour surfaces, the spatial dependency of  $(f - f_0)\beta_{\parallel}$  is removed through integration, where each radial point is weighted with the local current density times the surface of the flux surface. Accordingly,  $(f - f_0)\beta_{\parallel}$  represents the current distribution in momentum space, and the plasma

current can be computed by integrating over momentum space and multiplying with the elementary charge.

The momentum space current density is compared to the momentum-space sensitivity of a single channel for each of the two oblique ECE diagnostics, exactly like in figure 15, except that in figure 16(a), the considered distribution functions only account for quasi-linear electron cyclotron diffusion and collisions. In (b), the contour lines are the same as in figure 15.

In the ECCD-only case, a small portion of the momentum space current density is covered by the sensitivity of the oblique ECE. However, the coverage is insufficient to infer the entire plasma current. In the more realistic case depicted in (b), the coverage is even more limited. The majority of the current in the plasma is ohmic, and it resides at very low  $u_\perp$ , a region inaccessible to ECE in general. Nevertheless, the diagnostic approach might still have some potential for stellarators where no loop voltage exists.

## 6. Uncertainties and limitations of the current experiments

To obtain a quantitative match between the simulated ECE spectra and the measurements, a 1 cm downwards shift of all flux surfaces needed to be introduced into the equilibrium. There are four main sources of uncertainties that could explain the need for this shift: (1) the plasma parameters, (2) the 1/1 kink mode in the plasma center, (3) the considered models for radial transport, and (4), possible broadening of the ECRH beam due to turbulent scattering. Investigating the effect of the latter is beyond the scope of the current paper and will be the subject of future work. For medium devices like ASDEX Upgrade, the turbulent scattering is expected to be small [57]. The other three effects are discussed in the following sections.

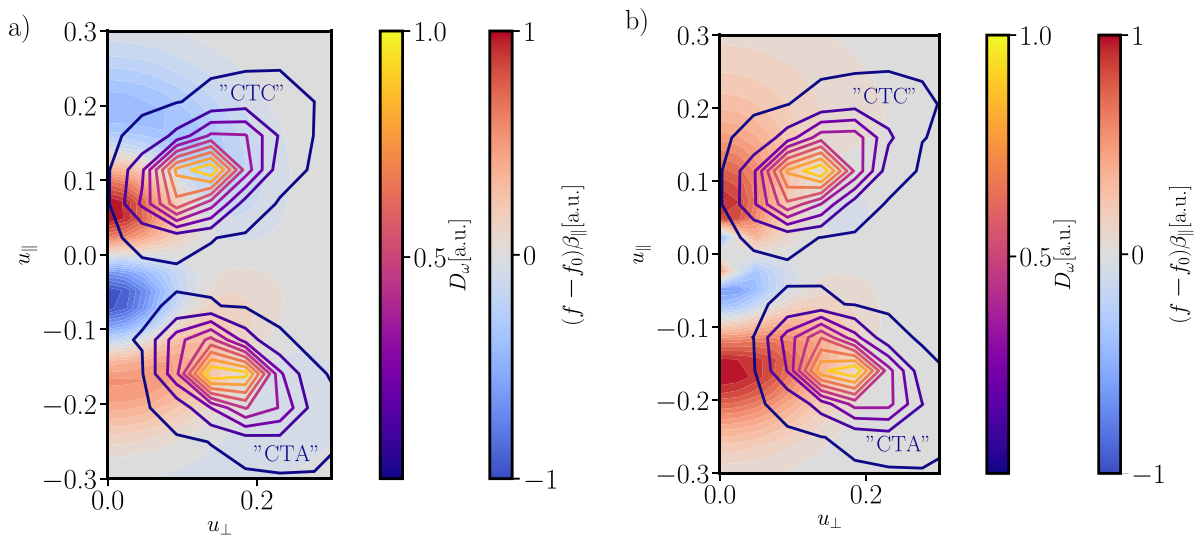


**Figure 16.** Comparison of the momentum-space sensitivity of the two oblique ECE diagnostics to the regions in momentum that contain the current in the plasma. In (a), only collisions, and ECCD are considered in the distribution function, while (b) considers the loop voltage, the radiation reaction force, and radial diffusion model C.

### 6.1. Equilibrium reconstruction and ECRH launcher angle

As shown in figure 2(a), the absorption of the ECRH beam occurs at  $R, z$ -positions different from the measurement positions of the oblique ECE. The ECRH deposition occurs above the magnetic axis, and the oblique ECE measures below it. ECRH deposition and ECE measurement volumes are not overlapping to avoid direct pick-up of ECRH launched power and frequency-shifted scattered light (from CTS) by the sensitive ECE receivers. The two volumes are linked by electron transport along the magnetic field, i.e. within flux surfaces. Nevertheless, this renders the interpretation of the measurements sensitive to the plasma elongation and the vertical position of the magnetic axis.

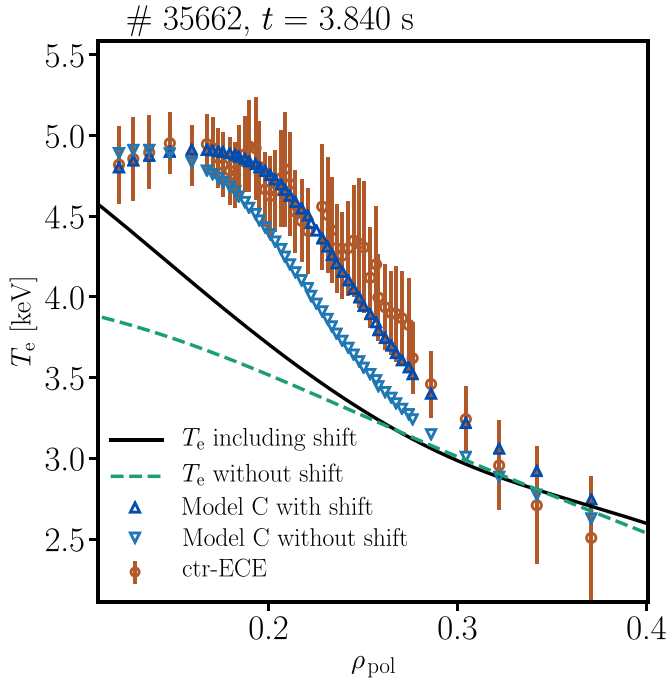
To minimize possible errors in the equilibrium reconstruction, the IDE [44] code was used for equilibrium reconstruction. It couples the Grad–Shafranov equation to the current diffusion equation to replace artificial smoothness constraints. For the kinetic pressure, it considers the  $T_e$  and  $n_e$  profiles computed through IDA and the thermal and fast ion pressures. The ion temperature is obtained via charge exchange recombination spectroscopy of boron ions [45]. Since there is no neutral beam power at  $t = 3.84$  s, the ion data from the short beam pulse at  $t = 4.2$  s is used for this time point. The fast-ion density is estimated via the RABBIT [47] code. One of the main strengths of IDE is the ability to include the measurements from current measuring diagnostics like the imaging motional Stark effect diagnostic [58] or plasma polarimetry [59]. Unfortunately, neither of these diagnostics can be properly used in the extremely low-density plasma scenario discussed in this paper. Hence, due to the lack of diagnostic coverage in the plasma center, the uncertainty of the  $z$ -position of the magnetic axis is estimated to be 6 mm by the IDE code.

In addition, to the uncertainty regarding the equilibrium, there is the possibility of errors in the assumed poloidal and toroidal angles of the ECRH launcher and oblique ECE

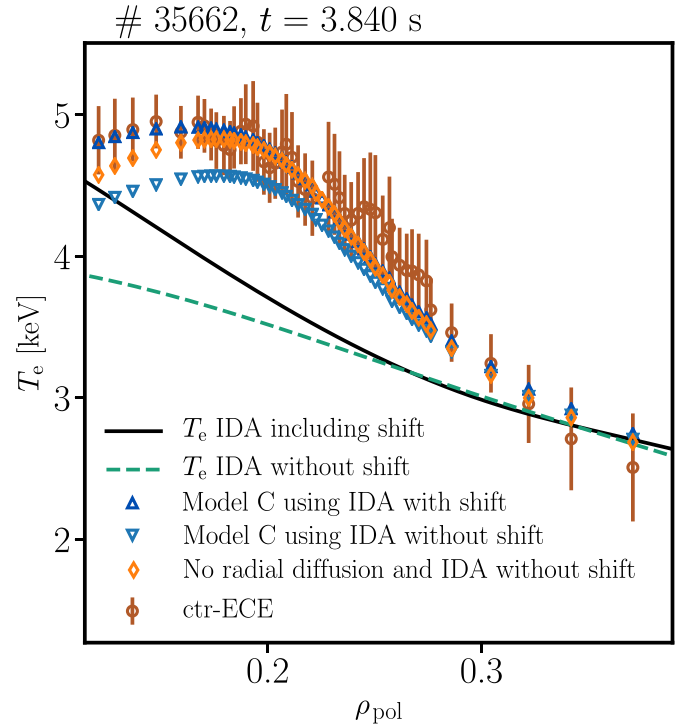
viewing mirrors. For the toroidal angles, these are of little consequence. For example, even an unlikely error as large as  $1^\circ$  changes the forward-modeled  $T_{\text{rad}}$  of the ctr-ECE by less than 100 eV. However, the uncertainty of the vertical beam/volume of sight position at the magnetic axis has not been assessed as of yet. There are two factors that play a role here. The first is a misalignment of the mirror itself, which is expected to be small and only produces uncertainties on the order of a few millimeters. The second more critical problem is the possible occurrence of parasitic modes in the wave guide. These arise due to either off-axis injection or axially asymmetric gyrotron output. This leads to a beat wave in the vessel that sweeps the beam laterally. Recent calculations with the PROFUSION code [60] showed a beat wave amplitude of about 1 cm, assuming that 10% of the power is coupled to a parasitic mode.

Figure 17 discusses the significance of the shift for the case of the RELAX distribution functions with model C for radial diffusion. It compares the synthetic data as shown in figure 7, i.e. with the vertical shift, to the synthetic ctr-ECE measurements obtained without the shift. The measurements of the diagnostic are also shown for reference. To reduce clutter in the graph, all measurements, synthetic and real, are mapped to the warm resonance positions obtained for the shifted equilibrium. For the original equilibrium, the majority of synthetic  $T_{\text{rad}}$  values fail to match the measurements, and the shape of the synthetic measurements is narrower than the measurements. Figure 17 also shows the  $T_e$  profiles obtained via IDA if the shift is considered or omitted in the analysis.

In conclusion, the uncertainty of the magnetic axis position and potential errors in the poloidal launch/viewing angle of the ECRH and oblique ECE systems pose a limiting factor to the interpretation of the experiments. The dependence on the vertical position of the magnetic axis could be eliminated in future experiments by matching the  $R$ - $z$  positions of the



**Figure 17.** Comparison between the ctr-ECE measurements and the synthetic  $T_{\text{rad}}$  based on radial diffusion model C, with and without a 1 cm vertical shift of the equilibrium. For the original equilibrium, the modeling underpredicts the majority of the measurements. The graph also shows the  $T_e$  profile that is obtained via IDA with the shift and the corresponding profile without it.



**Figure 18.** Comparison between the ctr-ECE measurements and the synthetic  $T_{\text{rad}}$  for different assumed  $T_e$  profiles. If the vertical shift is neglected when obtaining  $T_e$  via IDA, then the resulting  $T_{\text{rad}}$  can barely match the measurements in the absence of radial diffusion, but not for radial diffusion model C.

oblique ECE warm resonances and the deposition region of the gyrotron(s). To make the experiment more robust with regards to the uncertainties of the poloidal viewing/launching angles of the oblique ECE/ECRH, it would be useful to move the deposition further outwards. For flux surfaces with a larger diameter, an error on the order of several millimeters would only have small effect on the measurements. For such experiments, it would be necessary to strongly increase the ECRH power [11].

## 6.2. Uncertainty of $T_e$

Due to the particular shape of the plasma in #35662 at  $t = 3.84$  s, neither the Thomson scattering system nor the profile ECE covers the flux surfaces with  $\rho_{\text{pol}} < 0.15$ . Hence,  $T_e$  near the magnetic axis is unknown in this region. Since  $T_e$  is a critical quantity for the electron distribution function during ECCD, this is another limiting factor for the results shown in this paper. To illustrate the sensitivity to the adopted  $T_e$  profile, we compare the  $T_{\text{rad}}$  obtained with two  $T_e$  profiles. The first is consistently derived from the shifted equilibrium (c.f. figure 6), and for the second, the shift is neglected during the IDA. From these two  $T_e$  profiles, the distribution functions and the resulting  $T_{\text{rad}}$  are computed using the shifted equilibrium in both cases. Since two distinct  $T_e$  profiles are considered in RELAX, this also yields two unique sets of  $T_{\text{rad}}$ .

Figure 18 compares these sets of  $T_{\text{rad}}$  with the measurements of the ctr-ECE system. Again, both the synthetic and

real measurements are mapped to the warm resonance positions obtained with the  $T_e$  profile consistent with the shifted equilibrium. For the lower  $T_e$  profile, for which the shift is neglected, the  $T_{\text{rad}}$  including model C for radial diffusion fall short of the measurements at the plasma center. Even in the absence of radial diffusion, the synthetic  $T_{\text{rad}}$  underpredicts the measurements slightly (orange diamonds). If  $T_e$  is obtained consistently including the shift, then the resulting  $T_{\text{rad}}$  match the measurements if model C is considered for the radial diffusion.

## 6.3. Significance of the 1/1 kink mode

The ideal MHD kink mode rotating with about 2.6 kHz in the plasma center effectively smears out the ECRH deposition by shifting the flux surfaces. Its effect cannot be easily separated from the measurements through proper filtering, since it rotates much faster than the millisecond time scale that the modeled distribution function needs to achieve steady state. To assess the significance of the mode for the interpretation of the measurements, the magnitude of its displacement is derived from the modulation in  $\Delta T_{\text{rad}}$  that the mode causes in the radial ECE.

For an ECE channel with  $\rho_{\text{pol, res, cold}} = 0.3$ , the absolute magnitude of  $\Delta T_{\text{rad}} = 310$  eV. In the forward-modeled  $T_{\text{rad}}$  based on the average  $T_e$  profile, this corresponds to a shift of only  $\Delta \rho_{\text{pol}} = 0.03$ , or roughly 1.5 cm. Hence, this displacement is of the order of the vertical shift needed to get a match between experiment and modeling. Hence, the kink mode also

imposes an upper limit on the accuracy of the results. One solution to overcome this problem would be to avoid the occurrence of the mode in future experiments. This could be accomplished by using multiple gyrotrons with ctr-ECCD and by spreading out the power deposition such that the  $q$ -profile never falls below one. Alternatively, the smear-out effect of the ECRH deposition profile needs to be included in the modeling, which has been already been done with RELAX for neoclassical tearing modes [61].

#### 6.4. Turbulence models and the truncated collision operator

At present, very little is known about the momentum-space dependence of turbulent radial transport. An exception is reference [50] where gyrokinetic calculations were performed for mid-radius positions in ITER plasmas. These simulations show that it is most likely that the majority of the heat transport occurs at low momenta and inside the trapped cone. Of the three empirical radial diffusion models studied in this paper, Model C is the closest resemblance. This is encouraging since Model C after all delivers the best agreement between the modeling and the measurements. Nevertheless, the diffusion models investigated in this paper are certainly still very simplistic and leave much room for improvement.

Another potential weak point is the truncated collision operator, which acts as an infinite sink or source for energy. In reality, the power deposited by the ECRH is either radiated away or transported outwards, both of which lead to fluxes in phase space different from the flux caused by collisions with a thermal distribution function. Accordingly, an important step for future investigations would be the addition of a radiation model and to couple RELAX to a transport code to handle the radial heat transport properly. An energy-conserving collision operator is already available in RELAX.

## 7. Summary

Oblique ECE measurements were performed for ASDEX Upgrade discharge #35 662, a low density L-mode discharge subject to central ctr-ECCD. Electron distribution functions were computed with the RELAX code considering the ECRH beam parameters derived with the quasi-optical Gray code. The electron distribution function is not only a balance of collisions and electron cyclotron diffusion, but is also subject to the radial heat and particle transport. To test the sensitivity of oblique ECE on radial transport, four different models were considered, namely no diffusion, velocity-independent radial diffusion, and radial transport predominantly at either large or low electron momenta. For the radial dependence of the transport coefficients, the electron heat diffusivity was considered inside the plasma core. If the plasma is vertically shifted down by 1 cm, the oblique ECE measurements of both diagnostics are quantitatively matched only by the model considering radial transport at low electron energies. Out of the three considered models for the momentum space dependence of radial transport, this model has the closest resemblance to the gyrokinetic predictions for an ITER plasma.

Furthermore, the same trend has also been observed in a gyrokinetic calculations of a plasma in the TCV tokamak, which is similar to the discussed scenario.

It was shown that conventional, quasi-perpendicular ECE measurements cannot access the region in phase space where the ECRH power is absorbed. However, oblique ECE diagnostics viewing the plasma at the toroidal angle opposite to the ECRH and measuring closely around the gyrotron frequency can resolve the electron distribution function directly at the ECRH deposition site in phase space. Furthermore, an oblique ECE aligned with the ECRH toroidally can measure the abundance of electrons streaming in the direction opposite to the current drive. This allows the amount of pitch angle scattering and the effect of the loop voltage to be quantified. Nevertheless, oblique ECE diagnostics are unlikely to serve as a diagnostic for the plasma current in tokamaks. For stellarators, in which the loop voltage is zero, further investigations might be warranted.

Lastly, the limitations of the findings presented were discussed in detail. The empirical, vertical shift of the equilibrium is necessitated most likely by the combination of inaccurate equilibrium reconstruction, and errors in the vertical trajectory of the ECRH beam and the VOS of the oblique ECE. In addition, it was discussed how the uncertainty of the  $T_e$  profiles affects the synthetic measurements. Besides the possible errors in the plasma parameters the interpretation of the measurements is also limited by the presence of a 1/1 kink mode in the plasma center, which displaces the flux surfaces by 1.5 cm. The considered radial transport models and the truncated collision operator were identified as the main weaknesses of the modeling.

Oblique ECE accompanied by thorough modeling of the electron momentum distribution function and the radiation transport is a powerful tool for the experimental validation of electron cyclotron damping that has been left largely unexplored so far. Through improvement of the modeling tools and the experiment design, it could potentially be possible to even validate gyrokinetic predictions of the momentum space dependence of radial transport.

## Acknowledgments

One of the authors (S S Denk) acknowledges the valuable editorial input by J Cheng.

This work has been carried out within the framework of the EUROfusion Consortium and has received funding from the Euratom research and training programme 2014–2018 and 2019–2020 under Grant Agreement No. 633053. The views and opinions expressed herein do not necessarily reflect those of the European Commission.

## Appendix A. Oblique ECE cross-calibration

Since oblique ECE diagnostics are sensitive to Doppler-shifted emission, a direct cross-calibration against the absolutely calibrated profile ECE [36] at ASDEX Upgrade is not possible.



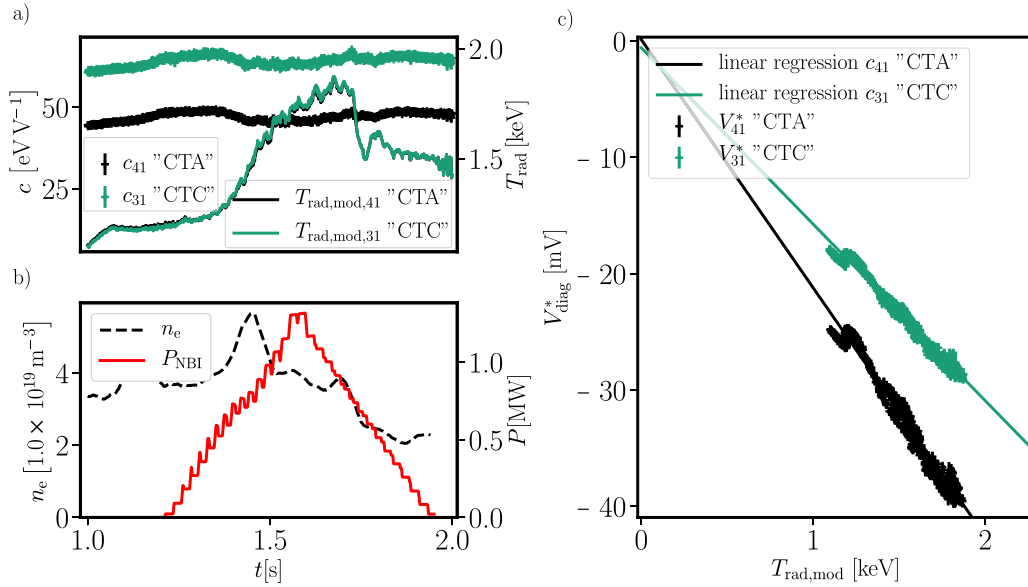


**Figure A1.** Summary of the cross-calibration of channel 41 of the ctr-ECE and channel 31 of the co-ECE for discharge # 35 662. (a) The time trace of the absolute value of the time-resolved calibration coefficients  $c_{41}(t)$  and  $c_{31}(t)$  (left y-axis) and the corresponding forward-modeled  $T_{\text{rad,mod}}$  which overlap. (b) NBI heating power (right y-axis) and  $n_e$  at the magnetic axis (left y-axis) as functions of time. (c) the linear regression of the measured signal  $V_{\text{diag}}^*$  vs.  $T_{\text{rad,mod}}$  for both channels.

Therefore, the diagnostic is cross-calibrated via the radiation transport code ECRad [28]. For the cross-calibration, it is important that the electron momentum distribution is thermal. In addition, it is beneficial if  $T_e$  is varied during the cross-calibration to quantify systematic errors. A detailed description of the cross-calibration process can be found in reference [28], in which the cross-calibration of channel 40 of the ctr-ECE was already discussed for discharge #35 662. However, for the sake of reproducibility, we show below the details on the cross calibration of both the ctr- and co-ECE for ASDEX Upgrade discharge #35 662 for two of the channels discussed in detail in section 5.

Figure A1 summarizes the cross-calibration process for channel 41 of the ctr-ECE and channel 31 of co-ECE. Figure A1(a) depicts the temporal evolution of the cross calibration factor  $c_{41}(t)$  and  $c_{31}(t)$  obtained for time point  $t$ . The corresponding radiation temperatures  $T_{41,\text{rad,mod}}$  and  $T_{31,\text{rad,mod}}$  are also shown using the right y-axis. Both calibration factors scatter at most about 5% around the time-averaged value. This is very close to the ideal case of a constant calibration factor. Note that all the plasma parameters entering the cross-calibration, i.e.  $T_e$ ,  $n_e$ , and the magnetic equilibrium are derived from measurements and are, therefore, uncertain. Both channels show the same temporal evolution, which makes it likely that the deviations from a perfectly constant calibration factor are not due to inherent problems with the diagnostics, but rather due to systematic errors of the plasma profiles and the equilibrium propagated to the calibration factor.

Figure A1(b) shows the heating power of the NBI system and  $n_e$  at the magnetic axis. The NBI heating was modulated such that it performed a triangular-shaped power scan. This results in a variation of  $T_e$ , which is necessary to get adequate estimates of the systematic uncertainties. Figure (c) shows the

linear regression of the diagnostic signal  $V_{\text{diag},41}^*$  and  $V_{\text{diag},31}^*$  against the predicted radiation temperature  $T_{\text{rad},41}$  and  $T_{\text{rad},31}$ . The linear regression matches the scatter plot well and, as expected, the regression shows that  $T_{\text{rad,mod}} = 0$  corresponds approximately to zero signal.

## Appendix B. Normalization of the different radial diffusion models

The three different models for the momentum dependence of the radial diffusion coefficients are normalized such that they produce the same radial heat flux at each radial point. This section uses spherical instead of cylindrical momentum space coordinates, i.e.  $(u, \theta)$ , with  $u$  the total dimensionless momentum, and  $\theta$  the pitch angle.

The starting point of the derivation is the radial transport equation considered in RELAX [14]

$$\frac{\partial \lambda' f}{\partial t} = \frac{1}{r} \frac{\partial}{\partial r} \left( r D_{\text{eff}} \frac{\partial}{\partial r} \lambda' f + r V_{\text{pinch,eff}} \lambda' f \right), \quad (\text{B1})$$

with  $f$  the electron momentum distribution function normalized to the local electron density  $n_e$ . The average minor radius of the flux surface  $r$  is given by  $\sqrt{V/2\pi^2 R}$ , with  $R$  the major radius, and  $V$  the flux surface volume.  $V_{\text{pinch,eff}} = \langle \nabla r \dot{V}_{\text{pinch}} \rangle_{\Psi}$  is the effective inward pinch velocity,  $V_{\text{pinch}}$  the diffusion velocity, and  $\langle \dots \rangle_{\Psi}$  indicates a flux surface average. Please see reference [14] for the definition  $\lambda'$ , which is not needed explicitly in the following.

The most important quantity in the current context is the effective diffusion coefficient  $D_{\text{eff}} = \langle (\nabla r)^2 D \rangle_{\Psi}$  where  $D$  is the diffusion coefficient. Since none of the three diffusion



models depends on the pitch angle, and the diffusion coefficients are assumed to be constant on a flux surface, the effective diffusion coefficient is

$$D_{\text{eff}} = \langle (\nabla r)^2 \rangle_{\Psi} D(r, u) \quad (\text{B2})$$

for all models. As noted in Ref [14], the effective inward pinch velocity is chosen such that it compensates for the particle flux due to the radial diffusion. Nevertheless, as long as the three diffusion models are properly normalized, this pinch velocity will be the same for all three of the models. Therefore, we can disregard the pinch term in equation (B1) when computing the normalization.

Next, we split the radial dependence of the diffusion coefficient from the momentum space dependence  $D = p(r)q(u)$  and introduce the electron momentum distribution function normalized to unity  $\hat{f} = f/n_e(r)$ .

$$\int \int \frac{1}{r} \frac{\partial}{\partial r} r \langle (\nabla r)^2 \rangle_{\Psi} p(r) q(u) \frac{\partial}{\partial r} \lambda' n_e(r) \hat{f}(r, u, \theta) 2\pi u^2 \sin(\theta) du d\theta = C(r), \quad (\text{B3})$$

with  $\theta$  the pitch angle and  $C(r)$  an arbitrary, momentum-independent function. Only the distribution function and  $q(u)$  are dependent on momentum space; hence, one can rewrite equation (B3)

$$\frac{1}{r} \frac{\partial}{\partial r} r \langle (\nabla r)^2 \rangle_{\Psi} p(r) \frac{\partial}{\partial r} \lambda' n_e(r) \iint q(u) \hat{f}(r, u, \theta) 2\pi u^2 \sin(\theta) du d\theta = C(r). \quad (\text{B4})$$

For model A,  $q_A(u) = 1$  and no normalization is needed

$$\frac{1}{r} \frac{\partial}{\partial r} r \langle (\nabla r)^2 \rangle_{\Psi} D_A(r) \frac{\partial}{\partial r} \lambda' \underbrace{\iint \hat{f}(r, u, \theta) 2\pi u^2 \sin(\theta) du d\theta}_{=1 \text{ for all } r} = C(r). \quad (\text{B5})$$

The normalization function for  $B(r)$  for model B can be derived from



$$\frac{1}{\mathcal{N}_B(r)} \iint \frac{u^2}{u_{\text{th},0}^2} \hat{f}(r, u, \theta) 2\pi u^2 \sin(\theta) du d\theta = 1 \text{ for all } r \quad (\text{B6})$$

and the normalization function  $C(r)$  for model C analogously from

$$\frac{1}{\mathcal{N}_C(r)} \iint \exp\left(-\frac{u^2}{4u_{\text{th},0}^2}\right) \hat{f}(r, u, \theta) 2\pi u^2 \sin(\theta) du d\theta = 1 \text{ for all } r. \quad (\text{B7})$$

## ORCID iDs

S S Denk  <https://orcid.org/0000-0002-9077-4610>  
 T Luda di Cortemiglia  <https://orcid.org/0000-0002-9941-0039>  
 J Hobirk  <https://orcid.org/0000-0001-6605-0068>  
 S K Nielsen  <https://orcid.org/0000-0003-4175-3829>

J Rasmussen  <https://orcid.org/0000-0002-3947-1518>  
 J Stober  <https://orcid.org/0000-0002-5150-9224>  
 M Willensdorfer  <https://orcid.org/0000-0002-1080-4200>

## References

- [1] Karney C and Fisch N 1981 *Nucl. Fusion* **21** 1549
- [2] Wagner D et al 2008 *Nucl. Fusion* **48** 054006
- [3] Lohr J et al 2005 *Fusion Sci. Technol.* **48** 1226
- [4] Ikeda Y et al 2002 *Fusion Sci. Technol.* **42** 435
- [5] Lee G et al 2000 *Nucl. Fusion* **40** 575
- [6] Takahashi H et al 2014 *Phys. Plasmas* **21** 061506
- [7] Hogge J-P, Alberti S, Porte L and Arnoux G 2003 *Nucl. Fusion* **43** 1353
- [8] Erckmann V et al 2007 *Fusion Sci. Technol.* **52** 291
- [9] Ramponi G, Farina D, Henderson M, Poli E, Saibene G and Zohm H 2007 *Fusion Sci. Technol.* **52** 193
- [10] Garavaglia S et al 2020 *Fusion Eng. Des.* **156** 111594
- [11] Harvey R W, McCoy M G and Kerbel G D 1989 *Phys. Rev. Lett.* **62** 426
- [12] Maj O, Poli E and Westerhof E 2012 *Joint Varenna-Lausanne Int. Workshop 2012 Journal of Conf. Series 13th Joint Varenna-Lausanne Int. Workshop on the Theory of Fusion Plasmas (Varenna, Italy, 27–31 August 2012)* vol 401 (Bristol: IOP Publishing)
- [13] Killeen J 1986 *Computational Methods for Kinetic Models of Magnetically Confined Plasmas (Springer Series in Computational Physics)* (Berlin: Springer)
- [14] Bertelli N and Westerhof E 2009 *Nucl. Fusion* **49** 095018
- [15] James R et al 1992 *Phys. Rev. A* **45** 8783
- [16] Harvey R W, O'Brien M R, Rozhddestvensky V V, Luce T C, McCoy M G and Kerbel G D 1993 *Phys. Fluids B* **5** 446
- [17] Petty C, Lin-Liu Y, Luce T, Makowski M, Prater R, Schuster D, John H S and Wong K 2001 *Nucl. Fusion* **41** 551
- [18] Petty C, Prater R, Lohr J, Luce T, Fox W, Harvey R, Kinsey J, Lao L and Makowski M 2002 *Nucl. Fusion* **42** 1366
- [19] Petty C, Austin M, Lohr J, Luce T, Makowski M, Prater R, Harvey R and Smirnov A 2010 *Fusion Sci. Technol.* **57** 10
- [20] Petty C et al 2003 *Nucl. Fusion* **43** 700
- [21] Coda S, Klimanov I, Alberti S, Arnoux G, Blanchard P, Fasoli A and the TCV team 2006 *Plasma Phys. Control. Fusion* **48** B359
- [22] Sozzi C, Bruschi A, Simonetto A, DeLaLuna E, Fessey J, Riccardo V and Contributors J-E et al 2005 *Fusion Eng. Des.* **74** 691
- [23] Preische S, Efthimion P C and Kaye S M 1996 *Phys. Plasmas* **3** 4065
- [24] Goodman T, Udintsev V, Klimanov I, Mueck A, Sauter O and Schlatter C 2008 *Fusion Sci. Technol.* **53** 196
- [25] De La Luna E, Krivenski V, Tudisco O, Amadeo P, Bruschi A, Gandini F, Granucci G, Muzzini V, FTU and E groups 2003 *Electron Cyclotron Emission and Electron Cyclotron Heating* (Singapore: World Scientific) pp 177–82
- [26] Volpe F, Austin M E, Campbell G and Deterly T 2012 *Rev. Sci. Instrum.* **83** 102502
- [27] Taylor G et al 2015 *EPJ Web of Conferences EDP Sciences* vol 87 p 03002
- [28] Denk S, Fischer R, Poli E, Maj O, Nielsen S, Rasmussen J, Stejner M and Willensdorfer M 2020 *Comput. Phys. Commun.* **253** 107175
- [29] Westerhof E, Peeters A and Schippers W 1992 RELAX: A computer code for the study of collisional and wave driven relaxation of the electron distribution function in toroidal geometry *Rijnhuizen Report* (FOM-Instituut voor Plasmafysica 'Rijnhuizen') ([https://aip.scitation.org/doi/suppl/10.1063/1.2727479/suppl\\_file/tr92-211.pdf](https://aip.scitation.org/doi/suppl/10.1063/1.2727479/suppl_file/tr92-211.pdf))

- [30] Farina D 2007 *Fusion Sci. Technol.* **52** 154 14th Joint Workshop on Electron Cyclotron Emission and Electron Cyclotron Resonance Heating, Santorini, Greece, May 09–12 2006
- [31] Poli E, Peeters A and Pereverzev G 2001 *Comput. Phys. Commun.* **136** 90
- [32] Poli E et al 2018 *Comput. Phys. Commun.* **225** 36
- [33] Nielsen S K et al 2015 *Plasma Phys. Control. Fusion* **57** 035009
- [34] Stejner M et al 2014 *Rev. Sci. Instrum.* **85** 093504
- [35] Hartfuss H J, Geist T and Hirsch M 1997 *Plasma Phys. Control. Fusion* **39** 1693
- [36] Denk S et al 2018 *Plasma Phys. Control. Fusion* **60** 105010
- [37] Willensdorfer M et al 2017 *Nucl. Fusion* **57** 116047
- [38] Denk S S et al 2016 *19th Joint Workshop (EC-19) on Electron Cyclotron Emission (ECE) and Electron Cyclotron Resonance Heating (ECRH)* EPJ
- [39] Fischer R, Fuchs C J, Kurzan B, Suttrop W, Wolfrum E and the ASDEX Upgrade Team 2010 *Fusion Sci. Technol.* **58** 675
- [40] Kurzan B and Murmann H D 2011 *Rev. Sci. Instrum.* **82** 103501
- [41] Mlynek A, Angioni C, Fable E, Fischer R, Ryter F, Stoiber J, Suttrop W, Zohm H and the ASDEX Upgrade Team 2012 *Nucl. Fusion* **52** 114012
- [42] Willensdorfer M, Wolfrum E, Fischer R, Schweinzer J, Sertoli M, Sieglin B, Veres G, Aumayr F and the ASDEX Upgrade Team 2012 *Rev. Sci. Instrum.* **83** eid023501
- [43] McCarthy P J, Martin P and Schneider W 1999 *The CLISTE Interpretive Equilibrium Code* (Cambridge, MA: Max-Planck)
- [44] Fischer R et al 2016 *Fusion Sci. Technol.* **69** 526
- [45] McDermott R et al 2017 *Rev. Sci. Instrum.* **88** 073508
- [46] Rathgeber S et al 2010 *Plasma Phys. Control. Fusion* **52** 095008
- [47] Weiland M et al 2018 *Nucl. Fusion* **58** 082032
- [48] Imbeaux F et al 2010 *Comput. Phys. Commun.* **181** 987
- [49] Pereverzev G V and Yushmanov P 2002 *Astra. Automated system for transport analysis in a tokamak IPP Report Max-Planck-Inst. für Plasmaphysik* ([https://pure.mpg.de/rest/items/item\\_2138238/component/file\\_2138237/content](https://pure.mpg.de/rest/items/item_2138238/component/file_2138237/content))
- [50] Casson F, Poli E, Angioni C, Buchholz R and Peeters A 2015 *Nucl. Fusion* **55** 012002
- [51] Told D private communication
- [52] Harvey R, Sauter O, Prater R and Nikkola P 2002 *Phys. Rev. Lett.* **88** 205001
- [53] Rasmussen J et al 2019 *Plasma Phys. Control. Fusion* **61** 095002
- [54] Albajar F, Bertelli N, Bornatici M and Engelmann F 2007 *Plasma Phys. Control. Fusion* **49** 15
- [55] Prater R 2004 *Phys. Plasmas* **11** 2349
- [56] Westerhof E and Kuznetsova L K 2007 *Plasma Phys. Control. Fusion* **49** 1509
- [57] Snicker A, Poli E, Maj O, Guidi L, Koehn A, Weber H, Conway G, Henderson M and Saibene G 2017 *Nucl. Fusion* **58** 016002
- [58] Ford O P, Burckhart A, McDermott R, Pütterich T, Wolf R C and the ASDEX Upgrade Team 2016 *Rev. Sci. Instrum.* **87** 11E537
- [59] Mlynek A, Casali L, Ford O, Eixenberger H and Team A U 2014 *Rev. Sci. Instrum.* **85** 11D408
- [60] Plaum B 2019 *Simulation of microwave beams with profusion* ([https://elib.uni-stuttgart.de/bitstream/11682/10269/1/Plaum\\_PROFUSION\\_2019.pdf](https://elib.uni-stuttgart.de/bitstream/11682/10269/1/Plaum_PROFUSION_2019.pdf))
- [61] Ayten B, Westerhof E et al 2014 *Nucl. Fusion* **54** 073001